

# Observation of unconventional many-body scarring in a quantum simulator

Guo-Xian Su (✉ [tspine@mail.ustc.edu.cn](mailto:tspine@mail.ustc.edu.cn))

University of Science and Technology of China

Hui Sun

University of Science and Technology of China

Ana Hudomal

University of Leeds

Jean-Yves Desaulles

University of Leeds

Zhaoyu Zhou

Bing Yang

Southern University of Science and Technology

Jad Halimeh

University of Trento

Zhen-Sheng Yuan

University of Science and Technology of China <https://orcid.org/0000-0003-4580-8225>

Zlatko Papic

University of Leeds <https://orcid.org/0000-0002-8451-2235>

Jian-Wei Pan

Shanghai Branch, National Laboratory for Physical Sciences at Microscale and Department of Modern Physics, University of Science and Technology of China <https://orcid.org/0000-0002-6100-5142>

---

## Article

### Keywords:

**Posted Date:** February 1st, 2022

**DOI:** <https://doi.org/10.21203/rs.3.rs-1220232/v1>

**License:**  This work is licensed under a Creative Commons Attribution 4.0 International License.

[Read Full License](#)

---

# Observation of unconventional many-body scarring in a quantum simulator

Guo-Xian Su,<sup>1,2,3</sup> Hui Sun,<sup>1,2,3</sup> Ana Hudomal,<sup>4</sup> Jean-Yves Desaulles,<sup>4</sup> Zhao-Yu Zhou,<sup>1,2,3</sup> Bing Yang,<sup>5</sup> Jad C. Halimeh,<sup>6</sup> Zhen-Sheng Yuan,<sup>1,2,3,\*</sup> Zlatko Papić,<sup>4,†</sup> and Jian-Wei Pan<sup>1,2,3,‡</sup>

<sup>1</sup>*Hefei National Laboratory for Physical Sciences at Microscale and Department of Modern Physics, University of Science and Technology of China, Hefei, Anhui 230026, China*

<sup>2</sup>*Physikalisches Institut, Ruprecht-Karls-Universität Heidelberg, Im Neuenheimer Feld 226, 69120 Heidelberg, Germany*

<sup>3</sup>*CAS Center for Excellence and Synergetic Innovation Center in Quantum Information and Quantum Physics, University of Science and Technology of China, Hefei, Anhui 230026, China*

<sup>4</sup>*School of Physics and Astronomy, University of Leeds, Leeds LS2 9JT, UK*

<sup>5</sup>*Department of Physics, Southern University of Science and Technology, Shenzhen 518055, China*

<sup>6</sup>*INO-CNR BEC Center and Department of Physics, University of Trento, Via Sommarive 14, I-38123 Trento, Italy*

(Dated: December 31, 2021)

The ongoing quest for understanding nonequilibrium dynamics of complex quantum systems underpins the foundation of statistical physics as well as the development of quantum technology. Quantum many-body scarring has recently opened a window into novel mechanisms for delaying the onset of thermalization, however its experimental realization remains limited to the  $\mathbb{Z}_2$  state in a Rydberg atom system. Here we realize unconventional many-body scarring in a Bose–Hubbard quantum simulator with a previously unknown initial condition – the unit-filling state. Our measurements of entanglement entropy illustrate that scarring traps the many-body system in a low-entropy subspace. Further, we develop a quantum interference protocol to probe out-of-time correlations, and demonstrate the system’s return to the vicinity of the initial state by measuring single-site fidelity. Our work makes the resource of scarring accessible to a broad class of ultracold-atom experiments, and it allows to explore its relation to constrained dynamics in lattice gauge theories, Hilbert space fragmentation, and disorder-free localization.

Coherent manipulation of quantum many-body systems far from equilibrium is key to unlocking outstanding problems in quantum sciences including strongly-coupled quantum field theories, exotic phases of matter, and development of enhanced metrology and computation schemes. These efforts, however, are frequently plagued by the presence of interactions in such systems, which lead to fast thermalization and information scrambling – the behavior known as quantum ergodicity [1–3]. A twist came with recent advances in synthetic quantum matter, which enabled detailed experimental study of thermalization dynamics in isolated quantum many-body systems, leading to the observation of ergodicity-violating phenomena in integrable [4] and many-body localized systems [5, 6].

More recently, quantum many-body scarring has emerged as another remarkable ergodicity-breaking phenomenon, where preparing the system in special initial states effectively traps it in a “cold” subspace that does not mix with the thermalizing bulk of the spectrum [7, 8]. Such behavior hinders the scrambling of information encoded in the initial state and suppresses the spreading of quantum entanglement, allowing a many-body system to display persistent quantum revivals. Many-body scarring was first observed in the Rydberg atom experimental platform [9, 10] and subsequent observations of weak ergodicity breaking phenomena have attracted much attention [11–13]. On the other hand, theoretical works have unearthed universal scarring mechanisms [14–

17], pointing to the ubiquity of scarring phenomena in periodically-driven systems [18–20] and in the presence of disorder [21, 22]. However, due to its high sensitivity to initial states and the fragility of quantum many-body systems, the experimental implementation of quantum many-body scars beyond the  $\mathbb{Z}_2$  state in Rydberg atom systems has remained elusive. It is thus vital to extend the realm of scarring to a greater variety of experimental platforms and more accessible initial conditions, which would empower fundamental understanding of nonergodic dynamics in various research areas ranging from lattice gauge theories to constrained glassy systems.

In this work, we observe many-body scarring in a large-scale Bose–Hubbard quantum simulator, where we employ a tilted optical lattice to emulate the PXP model, a canonical model of many-body scarring [23–26], see Fig. 1a. We demonstrate that a combination of detuning and periodic driving results in an unconventional many-body scarring regime in the unit-filling state, see Fig. 1b, hitherto believed to undergo fast thermalization [9]. Taking advantage of spin-dependent optical superlattices, we measure the system’s entanglement entropy by interfering identical copies in the double wells. We show the average entropy of single-site subsystems to be a good approximation of half-chain bipartite entropy, revealing a key property of scarring: the “trapping” of the quantum system in a low-entropy subspace, which prevents its relaxation into the exponentially large Hilbert space. Furthermore, we utilize the interference method to de-

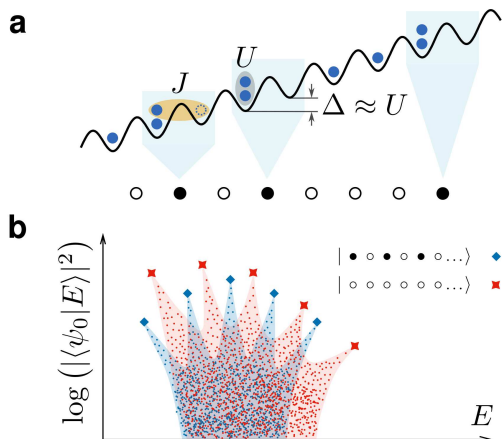


Figure 1. **Mapping the PXP model onto a Bose-Hubbard quantum simulator.** (a) At the  $U \approx \Delta \gg J$  resonance, the only allowed hopping process is  $11 \leftrightarrow 20$ . The PXP excitations,  $\bullet$ , live on the bonds between the lattice sites. The doublon configuration 20 in the Bose-Hubbard model maps to an excitation in the PXP model, while all other configurations are mapped to an empty site,  $\circ$ . For example, the given state  $|\dots \circ \bullet \bullet \circ \bullet \bullet \circ \bullet \dots\rangle$  maps to the Fock state  $|\dots 120201120\dots\rangle$ . (b) Scattered energy eigenstates  $|E\rangle$  (blue diamonds) are distinguished by their high overlap on a special initial state  $|\psi_0\rangle = |Z_2\rangle$ . By detuning the Bose-Hubbard model, we bias the spectrum and realize a new scarring regime associated with the polarized state,  $|0\rangle \equiv |\circ\circ\circ\dots\rangle$  (red crosses).

velop a protocol for measuring out-of-time correlations without brute-force tomography. We demonstrate this by measuring the single-site fidelity, which shows that scarring brings the system back to the vicinity of the initial state.

## OBSERVATION OF $Z_2$ QUANTUM MANY-BODY SCARS

We first benchmark our quantum simulator on  $Z_2$  quantum many-body scars [9]. We start by realizing the PXP model [27, 28], which describes a kinetically constrained chain of spin-1/2 degrees of freedom. Each spin can exist in two possible states,  $|\circ\rangle$ ,  $|\bullet\rangle$  corresponding to the ground state and excited state, respectively. An array of  $N$  such spins is governed by the Hamiltonian

$$\hat{H}_{\text{PXP}} = \Omega \sum_{j=1}^N \hat{P}_{j-1} \hat{X}_j \hat{P}_{j+1}, \quad (1)$$

where  $\hat{X} = |\circ\rangle\langle\bullet| + |\bullet\rangle\langle\circ|$  is the Pauli  $x$ -matrix, describing local spin precession with frequency  $\Omega$ . The projectors onto the ground state,  $\hat{P} = |\circ\rangle\langle\circ|$ , constrain the dynamics by allowing a spin to flip only if both of its neighbors are in the ground state.

In our quantum simulator, the PXP model is realized by tuning the on-site Hubbard interaction  $U$  to approx-

imately match the tilt potential  $\Delta$  of the optical lattice [29, 30], a regime that has been studied extensively in the context of quantum Ising chains [31–33]. In the resonant regime  $U \approx \Delta \gg J$ , where  $J$  is the hopping amplitude, three-boson occupancy of any site is strongly suppressed, and doublons can only be created by moving a boson to the left, e.g.,  $\dots 11 \dots \rightarrow \dots 20 \dots$ , or destroyed by moving a boson to the right, see Fig. 1a and Methods for details. The unit-filling state  $|111\dots\rangle$  maps to the PXP polarized state  $|0\rangle \equiv |\circ\circ\circ\dots\rangle$ , while the state with doublons on every other site,  $|2020\dots\rangle$ , corresponds to  $|Z_2\rangle \equiv |\bullet\circ\bullet\circ\dots\rangle$  state—the state containing the maximal number of excitations allowed by the constraint in the PXP model.

Remarkably, while the PXP model is quantum chaotic [23], preparing the system in a highly out-of-equilibrium  $|Z_2\rangle$  initial state leads to persistent quantum revivals [34–36]. The presence of revivals due to a special initial state in an overall chaotic system was understood to be a many-body analog of the phenomena associated with a single particle inside a stadium billiard, where nonergodicity arises as a “scar” imprinted by a particle’s classical periodic orbit [16, 37, 38]. In many-body scarred systems, eigenstates were shown to form tower structures, illustrated in Fig. 1b. These towers are revealed by the anomalously high overlap of eigenstates with the initial state, such as  $|Z_2\rangle$ , and their equal energy spacing is responsible for quantum revivals.

We initialize the experiment by employing a superlattice in the  $y$ -direction to prepare a  $\bar{n}=2$  Mott insulator in the left (odd) sites of the double wells with 99.2% fidelity, while removing all atoms on the right (even) sites via site-dependent addressing [39, 40]. This gives us the initial state  $|\psi_0\rangle = |Z_2\rangle = |2020\dots\rangle$  (see Methods). The superlattice is formed by super-imposing the “short” lattice, with  $a_s = 383.5$  nm spacing, and the “long” lattice, with  $a_l = 767$  nm spacing. In the region of interest, we have prepared 50 copies of the initial state  $|\psi_0\rangle$  isolated by the short lattice along the  $x$ -direction. Each copy extends over 50 short lattice sites along the  $y$ -direction. A pancake-shaped trap provides confinement in the  $z$ -direction. The short lattice in the  $y$ -direction makes an approximately  $4^\circ$  angle with gravity, which results in a static linear tilt per site of  $\Delta_g = 816$  Hz. An external magnetic field gradient can be generated with coils, creating a controllable linear tilting potential together with gravity.

After initial-state preparation, the atoms are isolated in deep lattices with  $60E_r$ .  $E_r = \hbar^2/8ma_s^2$  is the short-lattice recoil energy, where  $\hbar$  is the Planck constant and  $m$  is the  $^{87}\text{Rb}$  atomic mass. We quench the system out of equilibrium by abruptly dropping the  $y$ -lattice depth to  $11.6E_r$ , which corresponds to switching  $J$  from 0 to  $51(1)$  Hz. This is done while simultaneously adjusting the lattice depth in the  $x$  and  $z$ -directions accordingly, such that the interaction strength matches the linear tilt provided by gravity with  $U = \Delta_g \approx 16J$ . After evolution time  $t$ , we

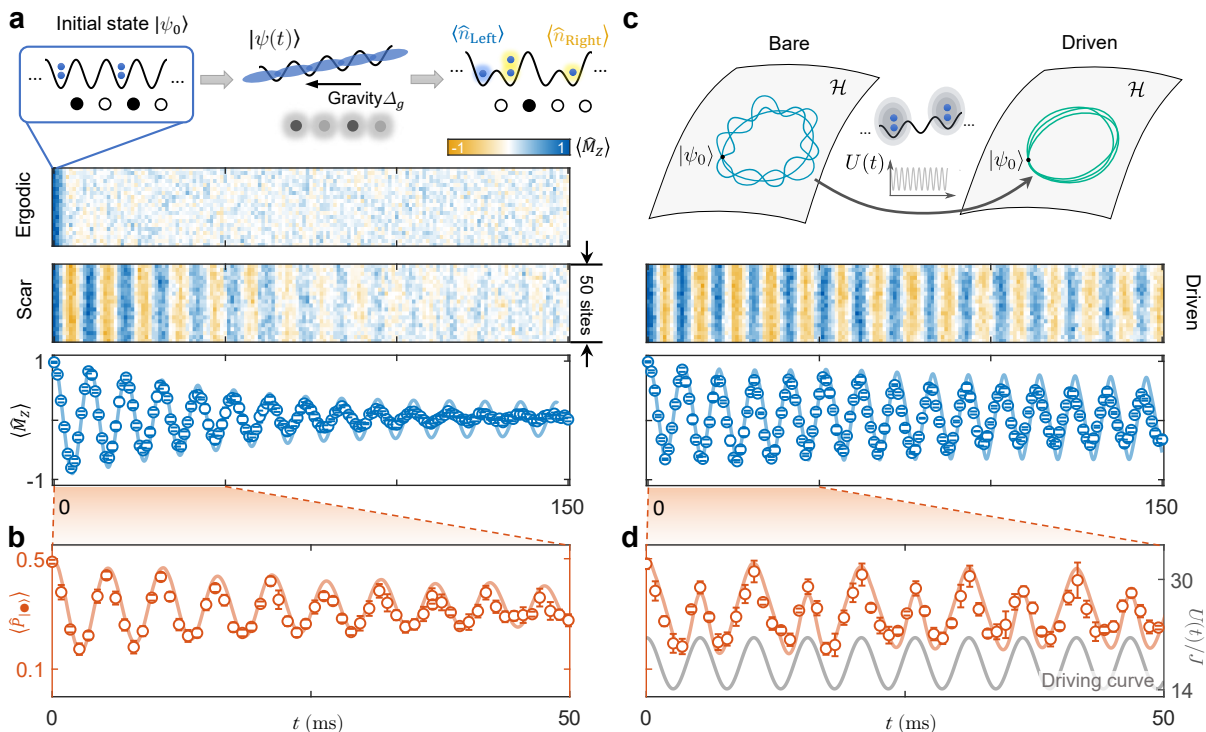


Figure 2. **Observation of  $\mathbb{Z}_2$  quantum many-body scars in a Bose-Hubbard quantum simulator.** (a)-(b) Starting from the state  $|\psi_0\rangle = |\dots 2020 \dots\rangle$ , the analog of  $|\mathbb{Z}_2\rangle$  state in the PXP model, we utilize gravity to provide linear tilt  $\Delta_g$ . We characterize quench dynamics by measuring density imbalance and the number of doublons, corresponding to staggered magnetization  $\langle \hat{M}_z \rangle$  and density of excitations  $\langle \hat{P}_{|\bullet\rangle} \rangle$  in the PXP model. In the detuned regime  $\Delta_g - U \approx -2J$ , the dynamics is ergodic and the system has no memory of the initial state at late times. By contrast, tuning to  $\Delta_g \approx U$ , we observe persistent oscillations in both  $\langle \hat{M}_z \rangle$  and  $\langle \hat{P}_{|\bullet\rangle} \rangle$ . This memory of the initial state is a signature of weak ergodicity breaking due to quantum many-body scars. (c)-(d) Periodic modulation of the interaction  $U(t) = \Delta + U_0 + U_m \cos(\omega t)$  with  $U_0 = 1.85J$ ,  $U_m = 3.71J$ ,  $\omega = 3.85J$  further suppresses the spreading of the wave function in the Hilbert space, leading to an enhancement of scarring. In both the static and driven case, experimental data for  $\langle \hat{M}_z \rangle$  and  $\langle \hat{P}_{|\bullet\rangle} \rangle$  are in excellent agreement with TEBD numerical simulations shown by blue and orange solid lines. Gray line shows the modulation  $U(t)$ .

1 freeze the dynamics and ramp up the double wells, where 22  
 2 we read out the atomic density on the left and right sites 23  
 3 of the  $y$ -superlattice successively with in-situ absorption 24  
 4 imaging [40, 41]. This provides access to density im- 25  
 5 balance,  $\langle \hat{M}_z \rangle = (\langle \hat{n}_{\text{Left}} \rangle - \langle \hat{n}_{\text{Right}} \rangle) / (\langle \hat{n}_{\text{Left}} \rangle + \langle \hat{n}_{\text{Right}} \rangle)$ , 26  
 6 an observable corresponding to the staggered magnetiza- 27  
 7 tion in the PXP model, see Fig. 2a. Another obser- 28  
 8 vable is the density of excitations in the PXP model, 29  
 9 which is measured by projecting the number occupancy 30  
 10 on each site into even (odd) parity, then reading out 31  
 11 the average odd particle density  $\langle \hat{P}_{|\bullet\rangle} \rangle_{(1)}$  [41]. Due 32  
 12 to highly suppressed multi-boson occupancy, we have 33  
 13  $\langle \hat{P}_{|\bullet\rangle} \rangle = \langle \hat{n}_{\text{doublon}} \rangle_{(1)} \approx (1 - \langle \hat{P}_{|\bullet\rangle} \rangle_{(1)}) / 2$ . 34

14 Away from the resonance, the dynamics is ergodic and 35  
 15 the staggered magnetization present in the initial  $|\mathbb{Z}_2\rangle$  36  
 16 state quickly decays with time, see Fig. 2a. In contrast, 37  
 17 in the vicinity of the resonance,  $\Delta = U$ , we observe distinct 38  
 18 signatures of scarring: the system approximately under- 39  
 19 goes persistent oscillations between the  $|\mathbb{Z}_2\rangle \equiv |\bullet\bullet\bullet\bullet\dots\rangle$  40  
 20 configuration and its partner shifted by one site,  $|\bar{\mathbb{Z}}_2\rangle \equiv$  41  
 21  $|\bullet\bullet\bullet\bullet\dots\rangle$ , as can be seen in the staggered magnetization 42

profile and the density of excitations in Fig. 2b. The den-  
 sity of excitations does not distinguish between  $|\mathbb{Z}_2\rangle$  and  
 $|\bar{\mathbb{Z}}_2\rangle$  states, hence there is a trivial factor of 2 difference  
 between the oscillation frequencies of  $\langle \hat{P}_{|\bullet\rangle} \rangle$  and  $\langle \hat{M}_z \rangle$ .

The scarred oscillations in Fig. 2a are visibly damped  
 with a decay rate  $\gamma$ , with  $\gamma^{-1} = 49.6 \pm 0.8$  ms. Neverthe-  
 less, as shown in Ref. [10], by periodically driving the sys-  
 tem it is possible to ‘refocus’ the spreading of the many-  
 body wavefunction in the Hilbert space and thereby en-  
 hance the scarring effect, as we demonstrate in Fig. 2c-  
 d. Crucially, this can be achieved without significantly  
 altering the period of revivals. Our driving protocol is  
 based on modulating the laser intensity of the  $z$ -lattice,  
 which translates into periodic modulation of the interac-  
 tion energy,  $U(t) = \Delta + U_0 + U_m \cos(\omega t)$ , while  $\Delta$  is kept  
 fixed. This results in a modulation of the density of dou-  
 blons in the chain, acting as the analog of the chemical  
 potential in the PXP model. For the driving parameters  
 in Fig. 2c we find a strong enhancement of the ampli-  
 tude of the oscillations in staggered magnetization with  
 $\gamma^{-1}$  increasing to  $208 \pm 10$  ms, while the period remains

1 nearly the same as in the static case. Optimal driving  
 2 parameters were determined numerically using a combi-  
 3 nation of simulated annealing and brute force search, see  
 4 Supplementary Material (SM).

5 We note that the experimental measurement of  $\langle \hat{M}_z \rangle$   
 6 damps slightly faster than the theory prediction, shown  
 7 by a line in Fig. 2a, at late times ( $t > 60$  ms). We attribute  
 8 this to an inherent residual inhomogeneity across the lat-  
 9 tice, which results in dephasing between different parts  
 10 of the system, as well as possible decoherence induced by  
 11 scattering of the lattice lasers. However, with driving we  
 12 observe a significant increase in coherence time (Fig. 2c).  
 13 To avoid the effect of these undesired dephasing or deco-  
 14 herence effects, in the following we limit our investigation  
 15 up to 60 ms.

### 16 UNRAVELING THE DETAILS OF SCARRED 17 DYNAMICS VIA QUANTUM INTERFERENCE

18 Fidelity and entanglement entropy are key observables  
 19 for characterizing scarring behavior. These observables  
 20 provide a window to the evolution of the system's wave  
 21 function and the spreading of quantum entanglement.  
 22 For a system trapped in a scarred subspace, thermal-  
 23 ization is inhibited and the system exhibits suppressed  
 24 entropy growth and periodic fidelity revivals. Measur-  
 25 ing these observables usually requires brute-force state  
 26 tomography, but for our 50-site Bose-Hubbard system  
 27 with a Hilbert space dimension exceeding  $10^{28}$ , this ap-  
 28 proach is generally impossible.

29 However, the superlattice in the  $x$ -direction allows us  
 30 to probe these observables by interfering identical copies  
 31 in the double wells, analogous to the 50 : 50 beam  
 32 splitter (BS) interference employed in photonics exper-  
 33 iments [42]; see Fig. 3a. This is done by freezing the  
 34 dynamics along the chains in the  $y$ -direction after evo-  
 35 lution time  $t$ , then we interfere copies of  $|\psi(t)\rangle$  in the  
 36 double wells formed by the  $x$ -superlattice (see Methods).  
 37 After the interference, a parity projection helps read out  
 38 the average odd particle density  $\langle \hat{P}_{\tilde{n} \in \text{odd}}^{\text{BS}} \rangle_{(1)}$ , which give  
 39 us access to the second-order Rényi entropy [43]. Due to  
 40 limitations in our imaging resolution, we were not able  
 41 to access entropy in extensively large subsystems, how-  
 42 ever, we measured the entropy of single-site subsystems  
 43  $S_{(1)} = -\ln(\text{Tr}_{(1)}[\hat{\rho}(t)^2]) = -\ln(1 - 2\langle \hat{P}_{\tilde{n} \in \text{odd}}^{\text{BS}} \rangle_{(1)})$ , where  
 44  $\hat{\rho}(t) = |\psi(t)\rangle \langle \psi(t)|$  is the density matrix. Due to the  
 45 strong suppression of entanglement growth in a scarred  
 46 system, we find  $S_{(1)}$  serves as a good approximation for  
 47 the half-chain bipartite entropy  $S_{L/2}$ , see Fig. 3b. Both  
 48 single-site and half-chain entropy are seen to oscillate  
 49 with the same frequency as  $\langle \hat{P}_{\bullet} \rangle$ , implying that the sys-  
 50 tem returns to the neighborhood of product states  $|\bar{Z}_2\rangle$   
 51 and  $|\bar{Z}_2\rangle$ . Our measurement of the Rényi entropy allows  
 52 to identify a driving protocol that almost fully discon-  
 53 nects the scarred subspace from the thermalizing bulk of  
 54 the spectrum, trapping the system in a vanishingly small

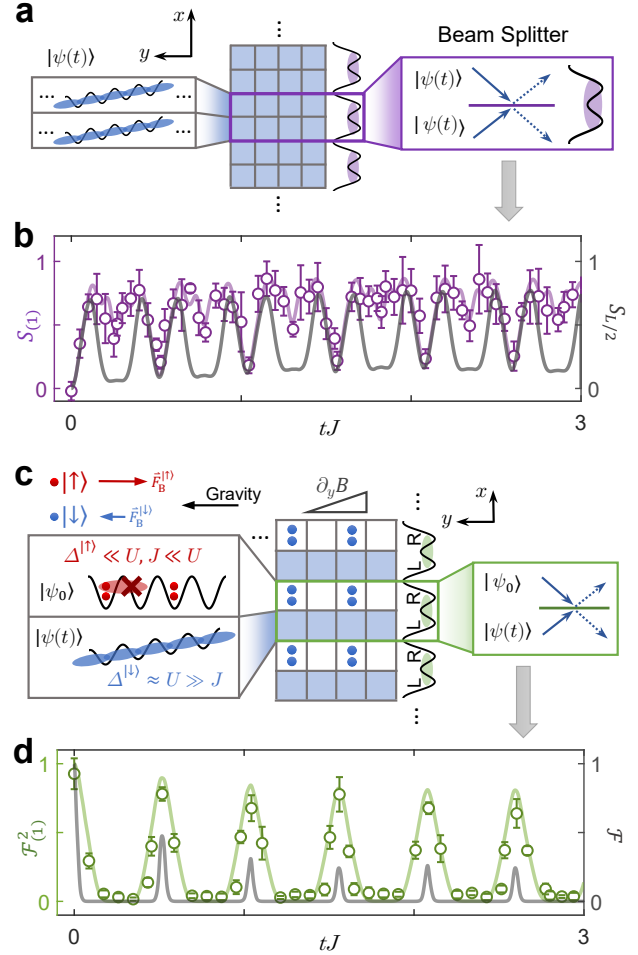


Figure 3. **Probing many-body scarred dynamics via quantum interference.** (a)-(b) After evolution time  $t$ , we freeze the dynamics in the  $y$ -direction, then by interfering two identical copies in the double wells along the  $x$ -direction, we obtain the second order Rényi entropy for a single site,  $S_{(1)}$ . The entropy is seen to have robust oscillations with the same frequency as in Fig. 2b, indicating a lack of thermalization at the single-site level. The single-site entropy is a good approximation to the half-chain entropy,  $S_{L/2}$ , evaluated numerically using TEBD (grey line). (c)-(d) We flip all right sites in the  $x$ -superlattice to the state  $|\uparrow\rangle$ , then by applying an external magnetic field gradient in the  $y$ -direction, we create state-dependent linear tilting with  $\Delta_B^{(\uparrow)} = -2\Delta_B^{(\downarrow)}$ . Fine tuning of the Hubbard parameters freezes the dynamics of  $|\uparrow\rangle$  atoms, which are flipped back to  $|\downarrow\rangle$  after evolution time  $t$ . We then interfere the left and right copies to read out single-site fidelity  $\mathcal{F}_{(1)}$ . The fidelity displays pronounced revivals, indicating periodic returns to the close vicinity of the initial state. Global fidelity, obtained numerically using TEBD, is shown by the grey line. Experimental data is for periodically driven systems with the same parameters as in Fig. 2d.

corner of an exponentially large Hilbert space.

Furthermore, we extend the interference protocol to probe unequal-time correlators. Before initiating the evolution, we first transfer atoms on the right sites of the

double wells in the  $x$ -superlattice to the internal state  $|\uparrow\rangle = |F=2, m_F = -2\rangle$  while leaving the atoms on the left sites in the state  $|\downarrow\rangle = |F=1, m_F = -1\rangle$ , see Methods for details. By applying the magnetic field gradient, we generate a state-dependent linear tilt with  $\Delta_B^{|\uparrow\rangle} = -2\Delta_B^{|\downarrow\rangle}$ , see Fig. 3c. We fine-tune the magnetic field gradient such that the  $|\uparrow\rangle$  atoms are effectively “frozen” in the initial state  $|\psi_0\rangle$ , while evolving the chains along the left sites to  $|\psi(t)\rangle$ . We then interfere these copies of  $|\psi_0\rangle$  and  $|\psi(t)\rangle$  in the  $x$ -superlattice, and thus read out the single-site fidelity with  $\mathcal{F}_{(1)} = \text{Tr}_{(1)}[\hat{\rho}_0\hat{\rho}(t)] = 1 - 2\langle\hat{P}_{n\in\text{odd}}^{\text{BS}}\rangle_{(1)}$ . In Fig. 3d, we observe that  $\mathcal{F}_{(1)}^2$  displays persistent revivals at the frequency of  $\langle\hat{M}_z\rangle$ , revealing the system’s periodic return to the vicinity of its initial state. The single-site fidelity  $\mathcal{F}_{(1)}$  provides an upper bound for the global fidelity  $\mathcal{F} = |\langle\psi_0|\psi(t)\rangle|^2$  for the quenches studied, and the two oscillate with the same frequency, as demonstrated numerically in Fig. 3d (see also SM).

### EMERGENCE OF AN UNCONVENTIONAL SCARRING REGIME

Remarkably, we find that a combination of detuning and periodic drive can result in dynamical stabilization of a distinct scarring regime for initial states other than  $|\mathbb{Z}_2\rangle$ . We highlight this finding in experimental observations of scarring behavior in the polarized state  $|0\rangle$ , previously not associated with quantum many-body scars [9].

We start with the unit-filling state  $|1111\dots\rangle$  in the lattice along the  $y$ -direction [39], which maps to the polarized state in the PXP model (see also Methods). In the absence of detuning or periodic drive, we observe fast relaxation: the density of excitations, single-site entropy, and fidelity all rapidly relax, with no visible oscillations beyond the timescale  $\sim 1/J$ , see Fig. 4a. Interestingly, when we bias the system by a static detuning,  $U_0 = -2.38J$ , we observe the emergence of oscillations in all three observables, accompanied by a slight decay, see Fig. 4b. Finally, if we also periodically modulate the interaction with amplitude  $U_m = 1.54J$  and frequency  $\omega = 4.9J \times 2\pi$ , we find a dramatic enhancement of scarring, Fig. 4c. In particular, both entropy and fidelity now show pronounced oscillations, signaling robust scar-induced coherence at all experimentally-accessible times.

Our experimental observations are explained by theoretical analysis of the PXP model summarized in Figs. 4d, e, f. By computing the overlap of all energy eigenstates  $|E\rangle$  of the PXP model in Eq. (1) with the polarized state  $|\psi_0\rangle = |0\rangle$ , we do not identify any hallmarks of scars, such as ergodicity-violating eigenstates with anomalously enhanced projection on  $|0\rangle$ , see Fig. 4d. On the other hand, when we add static detuning, which corresponds to the chemical potential in the PXP model, a band of scarred eigenstates with anomalously large overlap with  $|0\rangle$  emerges; see Fig. 4e. Numerical simulations show that the PXP model remains chaotic for the

value of static detuning used in experiment (Fig. 4b), and this detuning is not large enough to trivially fragment the entire spectrum into disconnected sectors with the given numbers of excitations (see SM). The band of scarred eigenstates, illustrated by crosses in Fig. 4e, spans the entire energy spectrum, but their support on  $|0\rangle$  is biased towards the ground state due to the breaking of particle-hole symmetry by detuning. We note that the scarred eigenstates in Fig. 4e are distinct from the known ones associated with the  $|\mathbb{Z}_2\rangle$  state, but otherwise possess similar scarring properties such as anomalously low entanglement entropy (see SM). Finally, further enhancement of scarring under periodic modulation of the PXP chemical potential is explained by the spectrum of the corresponding Floquet operator, numerically evaluated in Fig. 4f. We observe that a single Floquet mode (denoted by a cross) develops a very large overlap with the  $|0\rangle$  state. The existence of a single Floquet mode, whose mixing with other modes is strongly suppressed, gives rise to robust oscillations in the dynamics well beyond the experimentally accessible timescales.

### DISCUSSION AND OUTLOOK

We performed a quantum simulation of the paradigmatic PXP model of many-body scarring using a tilted Bose–Hubbard optical lattice. We demonstrated the existence of persistent quantum revivals from the  $|\mathbb{Z}_2\rangle$  initial state and their dynamical stabilization, opening up a new route for the investigation of scarring beyond Rydberg atom arrays. By harnessing the effect of detuning and periodic driving, we observed a distinct scarring regime associated with the polarized initial state. As the latter state is spatially homogeneous, its preparation does not require a superlattice, which makes further investigations of scarring phenomena accessible to a large class of ultracold atom experiments. The versatility of such platforms allows to directly probe the link between many-body scarring and other forms of ergodicity-breaking phenomena, such as Hilbert space fragmentation and disorder-free localization, as the latter can be conveniently studied in our setup by varying the tilt.

Our demonstration of scarring in the  $|0\rangle$  state highlights the importance of energy density. While the  $|\mathbb{Z}_2\rangle$  initial state has predominant support on the eigenstates in the middle of the spectrum, i.e., it constitutes an “infinite temperature” ensemble, the support of the  $|0\rangle$  state is biased towards one end of the spectrum as result of particle-hole symmetry breaking via the detuning potential. This suggests that, depending on the effective temperature, one can realize scarring from a much larger class of initial states with a suitable choice of detuning and periodic driving protocols (see SM). Furthermore, one may expect realizations of qualitatively new scarring models by tuning to other resonance conditions and other types of lattices, including ladders and two-dimensional

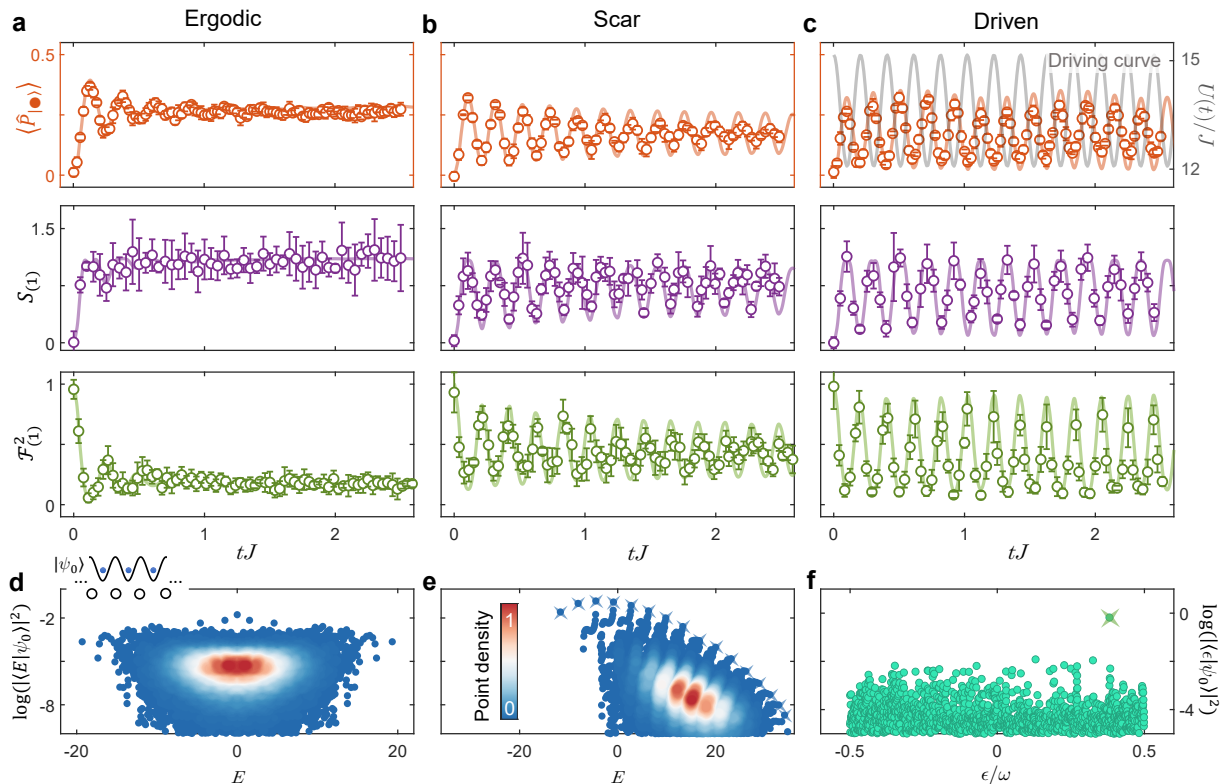


Figure 4. **Emergence of many-body scarring in the polarized state.** **a:** Fast thermalization from the unit-filling state in the Bose–Hubbard chain at  $U=\Delta$  resonance. **b:** Emergence of scarred dynamics in the presence of static detuning. **c:** Dynamical stabilization of scarred dynamics in the presence of both detuning and periodic driving. Panels **a**, **b**, **c** are experimental measurements of the density of excitations, second Rényi entropy and fidelity for a single site. Static detuning is  $U_0 = -2.38J$  and the modulation parameters are  $U_m=1.54J$ ,  $\omega=4.9J \times 2\pi$ . Lines are the results of TEBD simulations. **d**, **e**, **f:** Exact diagonalization results for the PXP model. **d**, **e** show overlaps of all eigenstates with the polarized state in the PXP chain on a ring with  $N=32$  sites. The value of static detuning in **e** matches that used in **b**. **f** shows the spectrum of the Floquet unitary for the PXP chain with  $N=24$  sites and driving parameters corresponding to **c**.

1 arrays. While in 1D our Bose–Hubbard lattice with the 22  
 2 staggered chemical potential can also be mapped to the 23  
 3 quantum link model providing a different PXP realiza- 24  
 4 tion [44], such a mapping does not directly extend to 25  
 5 higher dimensions and potentially results in yet another  
 6 class of scarred models. 26

7 Finally, our methods for probing unequal-time correla- 27  
 8 tors allow for state-of-the-art monitoring of nonequi- 28  
 9 librium dynamics and its applications in quantum tech- 29  
 10 nology. Notably, this protocol can be used to probe the 30  
 11 global fidelity, as well as the out-of-time correlations be- 31  
 12 tween arbitrary quantum states, e.g.,  $|\langle \psi(t_1) | \psi(t_2) \rangle|^2$ , 32  
 13 with the help of single-atom resolution quantum gas mi- 33  
 14 crosopes [43, 45]. This would empower detailed experi- 34  
 15 mental studies of exotic quantum phenomena such as dyn- 35  
 16 amical quantum phase transitions [46]. The observation 36  
 17 of long-lived quantum coherence due to scarring and its 37  
 18 controllable enhancement via periodic modulation, lays 38  
 19 the foundation for applications such as quantum mem- 39  
 20 ories and quantum sensing [47]. Moreover, the dynam- 39  
 21 ical manipulation of a many-body system employed in 40

this work can be directly used to prepare states with ex-  
 tensive multipartite entanglement [48], thus lending it-  
 self to novel protocols for phase estimation and quantum  
 metrology.

## ACKNOWLEDGMENTS

We thank Philipp Hauke, Bhaskar Mukherjee, and  
 Christopher Turner for useful discussions. The experi-  
 ment is supported by the NNSFC 12125409, the Anhui  
 Initiative in Quantum Information Technologies, and the  
 Chinese Academy of Sciences. A.H., J.-Y.D., and Z.P. ac-  
 knowledge support by EPSRC grant EP/R513258/1 and  
 by the Leverhulme Trust Research Leadership Award  
 RL-2019-015. A. H. acknowledges funding provided by  
 the Institute of Physics Belgrade, through the grant by  
 the Ministry of Education, Science, and Technological  
 Development of the Republic of Serbia. Part of the  
 numerical simulations were performed at the Scientific  
 Computing Laboratory, National Center of Excellence for  
 the Study of Complex Systems, Institute of Physics Bel-

grade. J.C.H. acknowledges support by Provincia Au-  
 tonoma di Trento, the ERC Starting Grant StrEnQTh  
 (project ID 804305), the Google Research Scholar Award  
 ProGauge, and Q@TN – Quantum Science and Technol-  
 ogy in Trento.

## AUTHOR CONTRIBUTIONS

G.-X.S., H.S., Z.-Y.Z., Z.-S.Y., and J.-W.P. performed  
 the experiment and analyzed the data. B.Y. participated  
 in the discussions and offered suggestions to the exper-  
 iment. A.H., J.Y.D., J.C.H., and Z.P. developed the  
 theoretical proposal for the experiment and performed  
 the theoretical analysis of the results. All authors con-  
 tributed to the writing of the manuscript.

## COMPETING INTERESTS

The authors declare no competing interests.

\* [yuanzs@ustc.edu.cn](mailto:yuanzs@ustc.edu.cn)

† [Z.Papic@leeds.ac.uk](mailto:Z.Papic@leeds.ac.uk)

‡ [pan@ustc.edu.cn](mailto:pan@ustc.edu.cn)

- [1] J. M. Deutsch, *Phys. Rev. A* **43**, 2046 (1991).
- [2] M. Srednicki, *Phys. Rev. E* **50**, 888 (1994).
- [3] M. Rigol, V. Dunjko, and M. Olshanii, *Nature* **452**, 854 (2008).
- [4] T. Kinoshita, T. Wenger, and D. S. Weiss, *Nature* **440**, 900 (2006).
- [5] R. Nandkishore and D. A. Huse, *Annual Review of Condensed Matter Physics* **6**, 15 (2015).
- [6] D. A. Abanin, E. Altman, I. Bloch, and M. Serbyn, *Rev. Mod. Phys.* **91**, 021001 (2019).
- [7] M. Serbyn, D. A. Abanin, and Z. Papić, *Nature Physics* **17**, 675 (2021).
- [8] S. Moudgalya, B. A. Bernevig, and N. Regnault, (2021), [arXiv:2109.00548 \[cond-mat.str-el\]](https://arxiv.org/abs/2109.00548).
- [9] H. Bernien, S. Schwartz, A. Keesling, H. Levine, A. Omran, H. Pichler, S. Choi, A. S. Zibrov, M. Endres, M. Greiner, V. Vuletić, and M. D. Lukin, *Nature* **551**, 579 (2017).
- [10] D. Bluvstein, A. Omran, H. Levine, A. Keesling, G. Semeghini, S. Ebadi, T. T. Wang, A. A. Michailidis, N. Maskara, W. W. Ho, S. Choi, M. Serbyn, M. Greiner, V. Vuletić, and M. D. Lukin, *Science* **371**, 1355 (2021).
- [11] W. Kao, K.-Y. Li, K.-Y. Lin, S. Gopalakrishnan, and B. L. Lev, *Science* **371**, 296 (2021).
- [12] S. Scherg, T. Kohlert, P. Sala, F. Pollmann, B. Hebbe Madhusudhana, I. Bloch, and M. Aidelsburger, *Nature Communications* **12**, 4490 (2021).
- [13] P. N. Jepsen, Y. K. Lee, H. Lin, I. Dimitrova, Y. Margalit, W. W. Ho, and W. Ketterle, “Catching Bethe-phantoms and quantum many-body scars: Long-lived spin-helix states in Heisenberg magnets,” (2021), [arXiv:2110.12043 \[cond-mat.quant-gas\]](https://arxiv.org/abs/2110.12043).
- [14] S. Moudgalya, N. Regnault, and B. A. Bernevig, *Phys. Rev. B* **98**, 235156 (2018).
- [15] N. Shiraishi and T. Mori, *Phys. Rev. Lett.* **119**, 030601 (2017).
- [16] W. W. Ho, S. Choi, H. Pichler, and M. D. Lukin, *Phys. Rev. Lett.* **122**, 040603 (2019).
- [17] D. K. Mark, C.-J. Lin, and O. I. Motrunich, *Phys. Rev. B* **101**, 195131 (2020).
- [18] S. Sugiura, T. Kuwahara, and K. Saito, *Phys. Rev. Research* **3**, L012010 (2021).
- [19] K. Mizuta, K. Takasan, and N. Kawakami, *Phys. Rev. Research* **2**, 033284 (2020).
- [20] B. Mukherjee, S. Nandy, A. Sen, D. Sen, and K. Sengupta, *Phys. Rev. B* **101**, 245107 (2020).
- [21] I. Mondragon-Shem, M. G. Vavilov, and I. Martin, *PRX Quantum* **2**, 030349 (2021).
- [22] N. Shibata, N. Yoshioka, and H. Katsura, *Phys. Rev. Lett.* **124**, 180604 (2020).
- [23] C. J. Turner, A. A. Michailidis, D. A. Abanin, M. Serbyn, and Z. Papić, *Nature Physics* **14**, 745 (2018).
- [24] C.-J. Lin and O. I. Motrunich, *Phys. Rev. Lett.* **122**, 173401 (2019).
- [25] T. Iadecola, M. Schecter, and S. Xu, *Phys. Rev. B* **100**, 184312 (2019).
- [26] V. Khemani, C. R. Laumann, and A. Chandran, *Phys. Rev. B* **99**, 161101 (2019).
- [27] P. Fendley, K. Sengupta, and S. Sachdev, *Phys. Rev. B* **69**, 075106 (2004).
- [28] I. Lesanovsky and H. Katsura, *Phys. Rev. A* **86**, 041601 (2012).
- [29] S. Sachdev, K. Sengupta, and S. M. Girvin, *Phys. Rev. B* **66**, 075128 (2002).
- [30] K. Sengupta, “Phases and dynamics of ultracold bosons in a tilted optical lattice,” (2021), [arXiv:2109.02657 \[cond-mat.quant-gas\]](https://arxiv.org/abs/2109.02657).
- [31] F. Meinert, M. J. Mark, E. Kirilov, K. Lauber, P. Weinmann, A. J. Daley, and H.-C. Nägerl, *Phys. Rev. Lett.* **111**, 053003 (2013).
- [32] F. Meinert, M. J. Mark, E. Kirilov, K. Lauber, P. Weinmann, M. Gröbner, A. J. Daley, and H.-C. Nägerl, *Science* **344**, 1259 (2014).
- [33] J. Simon, W. S. Bakr, R. Ma, M. E. Tai, P. M. Preiss, and M. Greiner, *Nature* **472**, 307 (2011).
- [34] B. Sun and F. Robicheaux, *New Journal of Physics* **10**, 045032 (2008).
- [35] B. Olmos, M. Müller, and I. Lesanovsky, *New Journal of Physics* **12**, 013024 (2010).
- [36] C. J. Turner, A. A. Michailidis, D. A. Abanin, M. Serbyn, and Z. Papić, *Phys. Rev. B* **98**, 155134 (2018).
- [37] E. J. Heller, *Phys. Rev. Lett.* **53**, 1515 (1984).
- [38] C. J. Turner, J.-Y. Desaulles, K. Bull, and Z. Papić, *Phys. Rev. X* **11**, 021021 (2021).
- [39] B. Yang, H.-N. Dai, H. Sun, A. Reingruber, Z.-S. Yuan, H.-N. Dai, Z.-S. Yuan, and J.-W. Pan, *Science* **369**, 550 (2020).
- [40] B. Yang, H.-N. Dai, H. Sun, A. Reingruber, Z.-S. Yuan, and J.-W. Pan, *Phys. Rev. A* **96**, 011602 (2017).
- [41] B. Yang, H. Sun, R. Ott, H.-Y. Wang, T. V. Zache, J. C. Halimeh, Z.-S. Yuan, P. Hauke, and J.-W. Pan, *Nature* **587**, 392 (2020).
- [42] A. M. Kaufman, M. C. Tichy, F. Mintert, A. M. Rey, and C. A. Regal, *Advances in Atomic, Molecular and Optical Physics*, 1st ed., Vol. 67 (Elsevier Inc., 2018) pp. 377–427, [arXiv:1801.04670](https://arxiv.org/abs/1801.04670).
- [43] R. Islam, R. Ma, P. M. Preiss, M. Eric Tai, A. Lukin, M. Rispoli, and M. Greiner, *Nature* **528**, 77 (2015).

- [44] F. M. Surace, P. P. Mazza, G. Giudici, A. Lerose, A. Gambassi, and M. Dalmonte, *Phys. Rev. X* **10**, 021041 (2020).
- [45] W. S. Bakr, J. I. Gillen, A. Peng, S. Fölling, and M. Greiner, *Nature* **462**, 74 (2009).
- [46] P. Jurcevic, H. Shen, P. Hauke, C. Maier, T. Brydges, C. Hempel, B. P. Lanyon, M. Heyl, R. Blatt, and C. F. Roos, *Phys. Rev. Lett.* **119**, 080501 (2017).
- [47] S. Dooley, *PRX Quantum* **2**, 020330 (2021).
- [48] J.-Y. Desaulles, F. Pietracaprina, Z. Papić, J. Goold, and S. Pappalardi, “Quantum many-body scars have extensive multipartite entanglement,” (2021), arXiv:2109.09724 [quant-ph].

## METHODS

### Mapping between PXP and Bose–Hubbard models

The Bose–Hubbard model in a tilted optical lattice is described by the Hamiltonian

$$\hat{H} = -J \sum_{i=1}^{L-1} \left( \hat{b}_i^\dagger \hat{b}_{i+1} + \hat{b}_{i+1}^\dagger \hat{b}_i \right) + \hat{U} + \hat{\Delta}, \quad (2)$$

where  $J$  is the hopping amplitude,  $\hat{b}$ ,  $\hat{b}^\dagger$  are the standard Bose annihilation and creation operators, the interaction energy is  $\hat{U} = (U/2) \sum_{i=1}^L \hat{n}_i (\hat{n}_i - 1)$ , and tilt potential is  $\hat{\Delta} = \Delta \sum_{i=1}^L i \hat{n}_i$ .  $L$  denotes the number of sites in the chain and we assume open boundary conditions. Moreover, we fix the filling factor to  $\nu=1$ , i.e., the total number of bosons is also equal to  $L$ .

In order to realize the PXP model in the Bose–Hubbard quantum simulator, we tune the parameters to the resonant regime  $U \approx \Delta \gg J$  [29, 30]. In this regime, three-boson occupancy of any site is strongly suppressed, and doublons can only be created by moving a particle

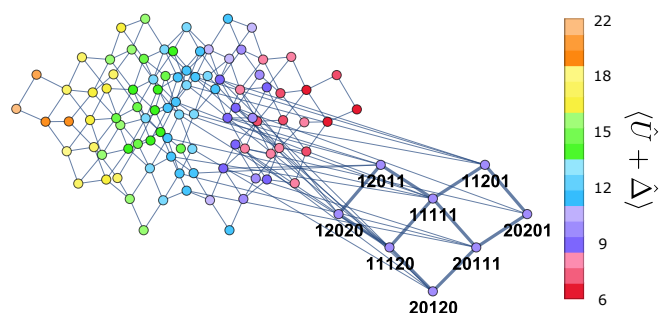


Figure M1. **Emergence of the PXP subspace in the Bose–Hubbard model at the resonance  $U \approx \Delta \gg J$ .** Dots represent Fock states of the tilted Bose–Hubbard model with 5 bosons on 5 sites (restricting to at most three bosons on any site). Lines denote the allowed hopping processes. The color scale shows the sum of interaction and tilt energies  $\langle \hat{U} + \hat{\Delta} \rangle$  for each Fock state, and this value is conserved by resonant processes. The PXP dynamical subspace and its Fock states are explicitly labeled.

to the left, e.g.,  $\dots 11 \dots \rightarrow \dots 20 \dots$ , or destroyed by moving a particle to the right. The states of the PXP model are understood to live on the bonds of the Bose–Hubbard model. An excitation in the PXP model  $\bullet_{j,j+1}$ , living on the bond  $(j, j+1)$ , corresponds to the creation of a doublon  $2_j 0_{j+1}$  on site  $j$  in the Bose–Hubbard chain. We identify the unit-filling state  $|111\dots\rangle$  with the PXP polarized state,  $|0\rangle \equiv |000\dots\rangle$ . Any other configuration of the PXP model can be mapped to a Fock state in the Bose–Hubbard model by starting from the unit-filling, identifying the bonds that carry PXP excitations and replacing the corresponding sites in the Mott state with  $11 \rightarrow 20$ , see SM for further details. Applying this rule across the chain allows to map any basis state of the PXP model to a corresponding Fock state in the Bose–Hubbard model, e.g., the  $|\mathbb{Z}_2\rangle$  state maps to the Fock state  $|\dots 2020 \dots\rangle$ . Fig. M1 illustrates the profound change in the connectivity of the Fock space near the resonance  $U \approx \Delta \gg J$ , with an emergent dynamical subspace isomorphic to the PXP model in the sector containing the  $|\mathbb{Z}_2\rangle$  state.

### State preparation and detection

Our experiment starts out with a two-dimensional Bose–Einstein condensate of  $^{87}\text{Rb}$  atoms prepared in the hyperfine state  $|\downarrow\rangle = 5S_{1/2} |F=1, m_F=-1\rangle$ . By applying a microwave pulse, atoms can be adiabatically transferred to the state  $|\uparrow\rangle = 5S_{1/2} |F=2, m_F=-2\rangle$ , which is resonant with the imaging laser and thus can be detected. The atoms are initially confined to a single layer of a pancake-shaped trap with  $3 \mu\text{m}$  period. In both  $x$  and  $y$ -directions, we have an optical superlattice that can be controlled separately. Each superlattice potential is generated by super-imposing two standing waves with laser frequency  $\lambda_s=767 \text{ nm}$  and  $\lambda_l=1534 \text{ nm}$ , which can be described by

$$\begin{aligned} V(x) &= V_s^x \cos^2(kx) - V_l^x \cos^2(kx/2 + \theta_x) \\ V(y) &= V_s^y \cos^2(ky) - V_l^y \cos^2(ky/2 + \theta_y), \end{aligned} \quad (3)$$

where  $V_s^{x(y)}$  is the depth of short (long) lattice in  $x(y)$ -direction,  $k=2\pi/\lambda_s$  is the short lattice wave number, and  $\theta_{x(y)}$  the relative phase between the short and long lattices in  $x(y)$ -direction.

We first perform a cooling technique by loading the atoms into a staggered superlattice in the  $y$ -direction at  $\theta_y=\pi/4$ , meanwhile ramping up only the short lattice in the  $x$ -direction. We tune the  $y$ -superlattice potential to create a Mott insulator with  $\bar{n}=2$  filling in odd sites, while even sites form a  $\bar{n}=1.5$  superfluid, serving as a reservoir for carrying away the thermal entropy [39].

Atoms in even sites are removed by performing site-selective addressing. This is done by first setting  $\theta_y=0$  to form double wells, then tuning the polarization of the short lattice laser along the  $y$ -direction to create an energy splitting between even and odd sites for the  $|\downarrow\rangle$  to

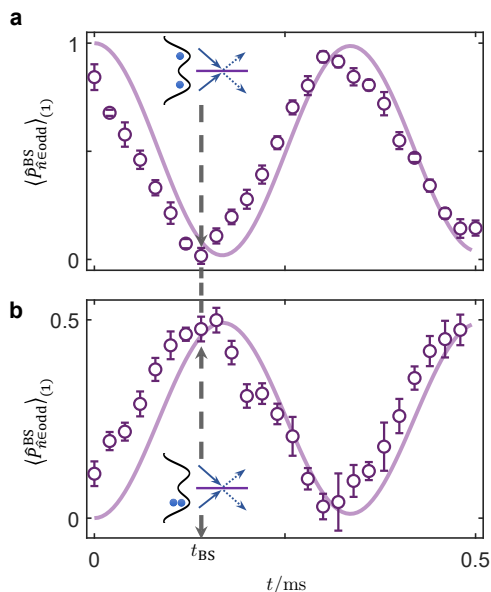


Figure M2. **Quantum interference.** (a) Interfering  $|1,1\rangle$  product states in the double wells. (b) Interfering  $|2,0\rangle$  product states in the double wells. Solid lines are TEBD simulations. Experimental data is shifted forward at earliest times due to the  $50 \mu\text{s}$  ramping time of the lattice potential.

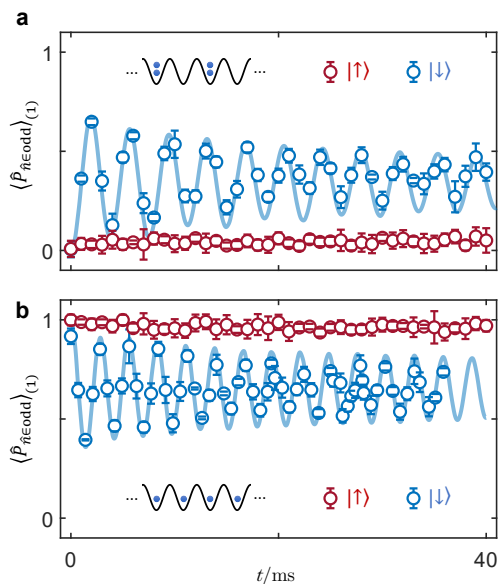


Figure M3. **Internal-state-dependent evolution.** (a) Starting from the initial  $|\mathbb{Z}_2\rangle$  state, chains with  $|\uparrow\rangle$  atoms remain largely at  $\langle \hat{P}_{\tilde{n} \in \text{odd}} \rangle_{(1)} \approx 0$  indicating they remain “frozen” in the initial state, while  $|\downarrow\rangle$  atoms evolve with the scarred dynamics. (b) Starting from the initial polarized state  $|0\rangle$ , chains with  $|\uparrow\rangle$  atoms remain largely at  $\langle \hat{P}_{\tilde{n} \in \text{odd}} \rangle_{(1)} \approx 1$ , while the  $|\downarrow\rangle$  atoms exhibit scarred dynamics in the presence of static detuning.

1  $|\uparrow\rangle$  transition. We transfer the atoms in even sites to  $|\uparrow\rangle$   
 2 and remove them with the imaging laser [40]. This way  
 3 we have prepared the initial  $|\mathbb{Z}_2\rangle$  state  $|2020\dots\rangle$ . The  
 4 same site-selective addressing procedure is also utilized  
 5 to read out atomic density on even and odd sites sep-  
 6 arately in experiment. Inside each isolated double-well  
 7 unit, we can perform state engineering that transfers the  
 8 state  $|2,0\rangle$  to  $|1,1\rangle$  [39]. This results in the unit-filling  
 9 state  $|1111\dots\rangle$  which corresponds to the polarized state  
 10  $|0\rangle$  in the PXP model.

### 11 Quantum interference in the double wells

12 The beam splitter (BS) interference is realized in the  
 13 balanced double wells formed by the superlattices in the  
 14  $x$ -direction, expressed in Eq. (3) by setting  $\theta_x=0$ . In the  
 15 non-interacting limit, indistinguishable bosonic particles  
 16 coming into the the interference at  $t=0$  interfere accord-  
 17 ing to the bosonic bunching. Therefore, equal number  
 18 of atoms coming into the two ports at  $t=0$  results in  
 19  $\langle \hat{P}_{\tilde{n} \in \text{odd}}^{\text{BS}} \rangle = 0$  at  $t_{\text{BS}}$ , while different number of atoms in-  
 20 terfering results in  $\langle \hat{P}_{\tilde{n} \in \text{odd}}^{\text{BS}} \rangle = 0.5$ . Each copy of atoms  
 21 coming into the interference are prepared individually,  
 22 hence no global phase between them, resulting in the  
 23 equivalence between the two output ports [43].

24 To implement the quantum interference protocol, we  
 25 quench the  $x$ -lattice potentials to  $V_s^x=6E_r$  and  $V_l^x=5E_r$ ,  
 26 resulting in the intra-double-well tunneling at  $J \approx 740$  Hz  
 27 and inter-double-well tunneling  $J' \approx 35$  Hz. Simultane-  
 28 ously, we lower the lattice depth in the  $x$ -direction to

25  $25E_r$  and trapping frequency in the  $z$ -direction to 1.4  
 kHz, achieving an interaction of  $U \approx 360$  Hz. Two exam-  
 26 ples are shown here in Fig. M2, where we interfere prod-  
 27 uct states  $|1,1\rangle$  (Fig. M2a) or  $|2,0\rangle$  (Fig. M2b) in the  
 28 double wells and read out the average odd particle  
 29 density. At  $t_{\text{BS}}=0.14$  ms we identify the beam splitter op-  
 30 eration, where  $|1,1\rangle$  gives  $\langle \hat{P}_{\tilde{n} \in \text{odd}}^{\text{BS}} \rangle_{(1)} = 0.01(3)$ , while  $|2,0\rangle$   
 31 gives  $\langle \hat{P}_{\tilde{n} \in \text{odd}}^{\text{BS}} \rangle_{(1)} = 0.48(3)$ . We simulate the interference  
 32 dynamics with a 20-site chain consisting of 10 double-  
 33 well units. We find good agreement at later times, while  
 34 the earlier times are affected by the finite time in the  
 35 lowering and rising of lattice potentials, which takes  $50$   
 36  $\mu\text{s}$ . The finite interaction strength and inter-double-well  
 37 tunneling results in about 1% error in the beam splitter  
 38 operation in the simulation, but this is beyond the  
 39 precision of our absorption imaging.

### Internal-state-dependent evolution

40 We use site-selective addressing in the  $x$ -superlattice  
 41 to transfer all right sites to the internal hyperfine state  
 42  $|\uparrow\rangle$  with a microwave pulse, while leaving all left sites in  
 43  $|\downarrow\rangle$  [40]. By applying an external magnetic-field gradient  
 44 in the  $y$ -direction  $\partial_y B$ , the magnetic energy shift between  
 45 nearest-neighbor short lattice sites of different hyperfine  
 46 states can be described by the anomalous Zeeman effect

$$47 \Delta_B^{|F,m_F\rangle} = \mu_B \times g_F \times m_F \times \partial_y B \times a_s, \quad (4)$$

1 where  $\mu_B$  is the Bohr magneton, the Landé factor  $g_F$   
 2 is 1/2 for  $|\uparrow\rangle$ , and -1/2 for  $|\downarrow\rangle$ . Therefore, we create  
 3 a state-dependent linear potential with  $\Delta_B^{|\uparrow\rangle} = -2\Delta_B^{|\downarrow\rangle}$ .  
 4 We fine-tune the gradient strength for different initial  
 5 conditions such that the total linear potential  $\Delta^{|\uparrow\rangle} =$   
 6  $\Delta_g^{|\uparrow\rangle} - |\Delta_B^{|\uparrow\rangle}| \ll U$  would avoid resonant processes while  
 7 suppressing the direct tunneling. Hence, atoms in the  $|\uparrow\rangle$   
 8 state are “frozen” in the initial states during the entire  
 9 evolution. To minimize the “leak” from the initial states,  
 10 the Hubbard parameters are optimized experimentally by  
 11 measuring the odd particle density  $\langle \hat{P}_{\hat{n} \in \text{odd}} \rangle_{(1)}$ . For the  
 12 initial  $|\mathbb{Z}_2\rangle$  state,  $\langle \hat{P}_{\hat{n} \in \text{odd}} \rangle_{(1)}$  should remain close to 0,  
 13 while for the polarized state  $|0\rangle$ ,  $\langle \hat{P}_{\hat{n} \in \text{odd}} \rangle_{(1)}$  should re-  
 14 main close to 1. We find the optimum magnetic field gra-  
 15 dient for  $|\mathbb{Z}_2\rangle$  state to be  $\partial_y B \approx 11.5$  G/cm, corresponding  
 16 to  $\Delta^{|\uparrow\rangle} \approx 200$  Hz, meanwhile, the  $|\downarrow\rangle$  atoms feel an in-  
 17 creased linear potential with  $\Delta^{|\downarrow\rangle} = \Delta_g^{|\downarrow\rangle} + |\Delta_B^{|\downarrow\rangle}| \approx 1120$   
 18 Hz, where we adjust the interaction  $U$  and tunneling  $J$   
 19 such that  $\Delta^{|\downarrow\rangle} \approx U \approx 16J$ , which give rise to the scarred dy-  
 20 namics, see Fig. M3a. For the polarized state, however,  
 21  $\partial_y B \approx 14.3$  G/cm and  $\Delta^{|\uparrow\rangle} \approx 50$  Hz results in better freez-  
 22 ing of the  $|\uparrow\rangle$  atoms, therefore we set  $U \approx \Delta^{|\downarrow\rangle} \approx 1200$  Hz,  
 23 see Fig. M3b. In both cases we find around 3% “leaking”  
 24 from the initial states within the investigation time we  
 25 measure single-site fidelity. This leaking contributes to  
 26 the small deviation in single-site fidelity we find between  
 27 experiments and TEBD simulations in Fig. 3 and Fig. 4.

28 After evolution time  $t$ , chains with  $|\downarrow\rangle$  atoms have  
 29 evolved to  $|\psi(t)\rangle$ , while chains with  $|\uparrow\rangle$  atoms have largely  
 30 remained in  $|\psi_0\rangle$ . We ramp up the short lattice in the  
 31  $y$ -direction to freeze the dynamics of  $|\downarrow\rangle$  atoms along the  
 32 chains, and flip all  $|\uparrow\rangle$  atoms back to  $|\downarrow\rangle$ . Then inter-  
 33 fere copies of  $|\psi_0\rangle$  and  $|\psi(t)\rangle$  in the double wells formed  
 34 by the  $x$ -superlattice. After the parity projection, we  
 35 read out single-site fidelity with  $\mathcal{F}_{(1)} = \text{Tr}_{(1)}[\hat{\rho}_0 \hat{\rho}(t)] =$   
 36  $1 - 2\langle \hat{P}_{\hat{n} \in \text{odd}}^{\text{BS}} \rangle_{(1)}$ .

— Supplementary Material —  
**Observation of unconventional many-body  
scarring in a quantum simulator**

**CONTENTS**

Mapping the tilted 1D Bose-Hubbard onto the PXP model

$\Delta \approx U$  resonance: first order terms  
Higher order terms in the mapping

Numerical methods

Numerical demonstrations of the mapping between PXP and tilted Bose-Hubbard model

Global vs. single-site fidelity

Alternative mapping between PXP and tilted 1D Bose-Hubbard with staggered detuning

Effect of periodic driving on  $\mathbb{Z}_2$  scars

Driven PXP model  
Driving the tilted 1D Bose-Hubbard model

Quantum many-body scars in the polarized state

Pure PXP model  
Static detuning in the PXP model  
Periodic driving in the PXP model  
Detuning and periodic driving in the tilted Bose-Hubbard model

Other quantum many-body scarred states

Effect of detuning on the spectral statistics of the PXP model

System-size scaling of the revival fidelity

References

**MAPPING THE TILTED 1D BOSE-HUBBARD  
ONTO THE PXP MODEL**

In the main text and throughout this Supplementary Material, we study the 1D Bose-Hubbard model with linear tilt potential and open boundary conditions, described by the Hamiltonian

$$\hat{H} = -J \sum_{i=1}^{L-1} \left( \hat{b}_i^\dagger \hat{b}_{i+1} + \hat{b}_{i+1}^\dagger \hat{b}_i \right) + \frac{U}{2} \sum_{i=1}^L \hat{n}_i (\hat{n}_i - 1) + \Delta \sum_{i=1}^L i \hat{n}_i, \quad (\text{S1})$$

$\underbrace{\hspace{10em}}_{\hat{H}_U} \qquad \underbrace{\hspace{10em}}_{\hat{H}_\Delta}$

where  $J$  is the hopping amplitude,  $U$  is the interaction strength,  $\Delta$  is the tilt and  $L$  the number of sites. Unless specified otherwise, we fix the filling factor to  $\nu = 1$ , i.e., the number of bosons is equal to the number of sites in the chain.

$\Delta \approx U$  resonance: first order terms

In the  $U, \Delta \gg J$  limit, the energy spectrum of the Hamiltonian in Eq. (S1) splits into bands with approximately constant expectation value of the diagonal terms,  $\langle \hat{H}_U + \hat{H}_\Delta \rangle \approx \text{const}$ , and the Hilbert space becomes fragmented. At the  $U \approx \Delta \gg J$  resonance, the only process which conserves  $\langle \hat{H}_U + \hat{H}_\Delta \rangle$  is  $11 \leftrightarrow 20$ , i.e. doublons can only be created by moving a particle to the left and destroyed by moving a particle to the right. In the connected component of the Fock state  $111 \dots 111$ , the system in the resonant regime can therefore be described by an effective Hamiltonian

$$\hat{H}_{\text{eff}} = -J \sum_{i=1}^{L-1} \left( \hat{b}_i^\dagger \hat{b}_{i+1} \hat{n}_i (2 - \hat{n}_i) \hat{n}_{i+1} (2 - \hat{n}_{i+1}) + \text{h.c.} \right). \quad (\text{S2})$$

The Hamiltonian (S2) is equivalent to the PXP Hamiltonian [S1, S2], as will be shown below (see also Ref. [S3] for the original derivation of the mapping and a recent review [S4]).

The connected component of the Hilbert space contains only certain types of two-site configurations (20, 11, 12, 02, 01), while all other two-site configurations are forbidden (22, 21, 10, 00). If we consider the configuration 20 to be an excitation, all allowed configurations can be mapped to those of the PXP model as follows:

$$\begin{aligned} \dots 20 \dots &\leftrightarrow \circ \bullet \circ \\ \dots 11 \dots &\leftrightarrow \circ \circ \circ \\ \dots 12 \dots &\leftrightarrow \circ \circ \bullet \\ \dots 02 \dots &\leftrightarrow \bullet \circ \bullet \\ \dots 01 \dots &\leftrightarrow \bullet \circ \circ \end{aligned} \quad (\text{S3})$$

Note that excitations live on the bonds between sites and this mapping also includes links to the two surrounding sites. For example, the configuration  $\dots 2020 \dots$  maps to  $\circ \bullet \circ \bullet \circ$  and not to  $\circ \bullet \circ \circ \bullet \circ$ . On the other hand, the configuration 2020 with open boundaries on both sides maps to  $\bullet \circ \bullet$ , as there are no bonds across the boundaries.

The effective Hamiltonian (S2) can be rewritten as:

$$\hat{H}_{\text{eff}} = -J \sum_{i=1}^{L-1} \left( \underbrace{\hat{b}_i^\dagger \hat{b}_{i+1} \delta_{\hat{n}_i, 1} \delta_{\hat{n}_{i+1}, 1}}_{\sqrt{2} \hat{P}_{j-1} \hat{\sigma}_j^+ \hat{P}_{j+1}} + \underbrace{\hat{b}_{i+1}^\dagger \hat{b}_i \delta_{\hat{n}_i, 2} \delta_{\hat{n}_{i+1}, 0}}_{\sqrt{2} \hat{P}_{j-1} \hat{\sigma}_j^- \hat{P}_{j+1}} \right). \quad (\text{S4})$$

1 In this equation, the index  $i$  labels the sites, while  $j$  labels 46  
 2 the bonds between sites. The Kronecker delta functions  
 3 have been expressed in terms of projectors,  $\hat{P}_j = |\circ_j\rangle\langle\circ_j|$ ,  
 4 and the bosonic hopping terms correspond to the spin  
 5 raising and lowering operators,  $\hat{\sigma}_j^\pm$ , on the bond  $j$ . We  
 6 can use delta functions because there are no configura-  
 7 tions with more than 2 particles per site in this connected  
 8 component and the only possible values of  $\hat{n}_i(2 - \hat{n}_i)$  are  
 9 0 and 1. Moving a particle to a neighboring site on the  
 10 left corresponds to creating an excitation, moving to the 47  
 11 right to annihilating, while the delta functions act as con- 48  
 12 straints.

13 Finally, the effective Hamiltonian is therefore equiva-  
 14 lent to the PXP Hamiltonian

$$\begin{aligned} \hat{H}_{\text{PXP}} &= \Omega \sum_{j=1}^N \left( \hat{P}_{j-1} \hat{\sigma}_j^+ \hat{P}_{j+1} + \hat{P}_{j-1} \hat{\sigma}_j^- \hat{P}_{j+1} \right) \\ &= \Omega \sum_{j=1}^N \hat{P}_{j-1} \hat{X}_j \hat{P}_{j+1}, \end{aligned} \quad (\text{S5})$$

15 when  $\Omega = \sqrt{2}J$  and  $N = L - 1$ , where  $\hat{X}_j \equiv |\circ_j\rangle\langle\bullet_j| + 53$   
 16  $|\bullet_j\rangle\langle\circ_j|$  is the usual Pauli  $x$  matrix. In case of open 54  
 17 boundary conditions (OBC) the two boundary terms be-  
 18 come  $\hat{X}_1 \hat{P}_2$  and  $\hat{P}_{N-1} \hat{X}_N$ . Note that the effective bosonic  
 19 model for system size  $L$  is equivalent to the PXP model  
 20 for size  $N = L - 1$  since the number of bonds is the  
 21 number of sites minus one.

22 In the PXP model, the initial states which lead to  
 23 pronounced quantum revivals are the two states with  
 24 the maximal number of excitations – the Néel states,  
 25  $\bullet\bullet\bullet\bullet\dots\bullet\bullet$  and  $\circ\circ\circ\circ\dots\circ\circ$  [S5, S6]. The equivalent states  
 26 in the tilted Bose-Hubbard model are 2020...201 and  
 27 12020...20 for odd system sizes and 2020...20 and 55  
 28 120...201 for even sizes. In our experimental setup, it is 56  
 29 not possible to exactly prepare the 2020...201 state due 57  
 30 to the inability to independently control single sites. In- 58  
 31 stead, our experiment realizes the 2020...20 state, which 59  
 32 corresponds to the Néel state  $\bullet\bullet\bullet\bullet\dots\bullet\bullet$  in the PXP 60  
 33 model with an odd number of sites and open boundary 61  
 34 conditions.

### 35 Higher order terms in the mapping

36 The effective Hamiltonian of Eq. (S2) results from  
 37 the first-order Schrieffer-Wolff transformation [S7] where  
 38  $\hat{H}_0 = \hat{H}_U + \hat{H}_\Delta$ . In this section we look at the relevant  
 39 terms that arise in the effective Hamiltonian at second  
 40 order. To simplify the notation we write these terms as  
 41 sums of range-3 operators, where  $|111\rangle\langle 120|_j$  denotes the  
 42 operator changing sites  $j-1$ ,  $j$  and  $j+1$  from 120 to 111  
 43 while leaving all other sites unaffected.

44 First, we can identify the matrix elements that take  
 45 the system out of the PXP sector. This happens by the

appearance of sites with 3 bosons via the operator

$$\begin{aligned} \hat{H}_{\text{out}} &= \frac{\sqrt{3}J^2}{U} \sum_{j=2}^{L-1} \left( |300\rangle\langle 201|_j + |201\rangle\langle 300|_j \right. \\ &\quad \left. + 2|300\rangle\langle 120|_j + 2|120\rangle\langle 300|_j \right). \end{aligned} \quad (\text{S6})$$

There are also off-diagonal matrix elements connecting  
 states within the PXP sector, given by

$$\hat{H}_{\text{OD}} = \frac{2J^2}{U} \sum_{j=2}^{L-1} \left( |120\rangle\langle 201|_j + |201\rangle\langle 120|_j \right). \quad (\text{S7})$$

There are also additional off-diagonal matrix elements  
 connecting states outside of the PXP sector, but as they  
 do not directly influence the dynamics out of it we do not  
 describe them here.

Finally, the diagonal operator in this sector is given by

$$\begin{aligned} \hat{H}_{\text{Diag}} &= \frac{J^2}{U} \sum_{j=2}^{L-1} \left( 4|120\rangle\langle 120|_j - |111\rangle\langle 111|_j \right. \\ &\quad \left. + |020\rangle\langle 020|_j - |112\rangle\langle 112|_j \right) \\ &\quad + \frac{J^2}{U} \left( |01\rangle\langle 01|_{L-1} - |11\rangle\langle 11|_1 - |12\rangle\langle 12|_1 \right), \end{aligned} \quad (\text{S8})$$

where the two-site operator  $|11\rangle\langle 12|_j$  acts on sites  $j$  and  
 $j+1$ . As bulk terms get added, the overall diagonal  
 factors are extensive in the system size in the Fock basis.  
 The state with the lowest on-site potential is  $|111\dots 11\rangle$   
 with a value of  $-\frac{(L-1)J^2}{U}$ . The maximum is  $\approx \frac{4J^2L}{3U}$  for  
 the state  $|120120\dots 120\rangle$ , which corresponds to the  $\mathbb{Z}_3$   
 state in the PXP terminology.

In order to see how these second-order terms change  
 the effective model we can rewrite Eqs. (S7)-(S8) for  
 the PXP model with  $N = L - 1$  sites. To do this we  
 introduce the single-site projector on the excited state  
 $\hat{Q}_j = |\bullet\rangle\langle\bullet| = \mathbf{1} - \hat{P}_j$ . We then obtain

$$\begin{aligned} \hat{H}_{\text{OD}}^{\text{PXP}} &= \frac{2J^2}{U} \sum_{j=1}^{N-2} \left( \hat{P}_{j-1} \hat{\sigma}_j^+ \hat{\sigma}_{j+1}^- \hat{P}_{j+2} + \hat{P}_{j-1} \hat{\sigma}_j^- \hat{\sigma}_{j+1}^+ \hat{P}_{j+2} \right) \\ &\quad + \frac{2J^2}{U} \left( \hat{\sigma}_1^+ \hat{\sigma}_2^- \hat{P}_3 + \hat{\sigma}_1^- \hat{\sigma}_2^+ \hat{P}_3 \right) \\ &\quad + \frac{2J^2}{U} \left( \hat{P}_{N-3} \hat{\sigma}_{N-1}^+ \hat{\sigma}_N^- + \hat{P}_{N-2} \hat{\sigma}_{N-1}^- \hat{\sigma}_N^+ \right) \end{aligned} \quad (\text{S9})$$

1 and

$$\begin{aligned}
\hat{H}_{\text{Diag}}^{\text{PXP}} = & \frac{J^2}{U} \sum_{j=1}^{N-2} (4\hat{P}_{j-1}\hat{P}_j\hat{Q}_{j+1}\hat{P}_{j+2} - \hat{P}_{j-1}\hat{P}_j\hat{P}_{j+1}\hat{P}_{j+2} \\
& + \hat{Q}_{j-1}\hat{P}_j\hat{Q}_{j+1}\hat{P}_{j+2} - \hat{P}_{j-1}\hat{P}_j\hat{P}_{j+1}\hat{Q}_{j+2}) \\
& + \frac{J^2}{U} (4\hat{P}_0\hat{Q}_1\hat{P}_2 - \hat{P}_0\hat{P}_1\hat{P}_2 - \hat{P}_0\hat{P}_1\hat{Q}_2 \\
& + 4\hat{P}_{N-2}\hat{P}_{N-1}\hat{Q}_N - \hat{P}_{N-2}\hat{P}_{N-1}\hat{P}_N \\
& + \hat{Q}_{N-2}\hat{P}_{N-1}\hat{Q}_N) \\
& + \frac{J^2}{U} (\hat{Q}_{N-1}\hat{P}_N - \hat{P}_0\hat{P}_1 - \hat{P}_0\hat{Q}_1),
\end{aligned} \tag{S10}$$

2 respectively. We notice that the off-diagonal correction  
3 has the form of a constrained XY term.

#### 4 NUMERICAL METHODS

5 In the main text and this Supplementary Material, we  
6 use two types of numerical methods for modeling the ex-  
7 periment. For small Bose-Hubbard chains with  $L \lesssim 12$   
8 sites, we use exact diagonalization techniques to obtain  
9 the full energy spectrum of the Hamiltonian and directly  
10 access the system's eigenstate properties. Unless speci-  
11 fied otherwise, we restrict the occupancy of any site to  
12 be at maximum 3 bosons, as our results are found to be  
13 insensitive to allowing more than 3 bosons on any site.

14 To access dynamics in much larger systems,  $L \lesssim 50$   
15 sites, we use TEBD variational method [S8] implemented  
16 in TenPy package [S9]. We employ the second order Trot-  
17 ter decomposition with time step  $2.5 \times 10^{-5}/J$  and max-  
18 imum bond dimension  $\chi_{\text{max}} = 3000$ . Such a small time  
19 step was necessary because some of the quantities we  
20 are interested in, e.g., the fidelity density, are sensitive  
21 to otherwise negligible fluctuations in the revival peak  
22 heights that appear for longer time steps.

23 For numerical simulations via either one of these meth-  
24 ods, it is convenient to work in natural units  $\hbar=1$ . We  
25 adopt this convention for presenting all numerical results  
26 in this Supplementary Material.

#### 27 Numerical demonstrations of the mapping between 28 PXP and tilted Bose-Hubbard model

29 In this Section, we numerically corroborate the map-  
30 ping between PXP and Bose-Hubbard models intro-  
31 duced in Sec. . Specifically, we use exact diagonalization  
32 to demonstrate the consistency between dynamics and  
33 eigenstate properties in the PXP model and the Bose-  
34 Hubbard model tuned to the resonance  $U=\Delta$ . 42

35 In analogy with the PXP model, the system initialized 43  
36 in the state  $2020\dots 201$  is expected to oscillate 44  
37 this state and the state  $12020\dots 20$ . This is not only the 45

38 case for the effective model (S4) which is exactly equiv-  
39 alent to PXP, but also for the full tilted Bose-Hubbard  
40 model (S1) at the  $U = \Delta$  resonance, as can be observed  
41 in Fig. S1.

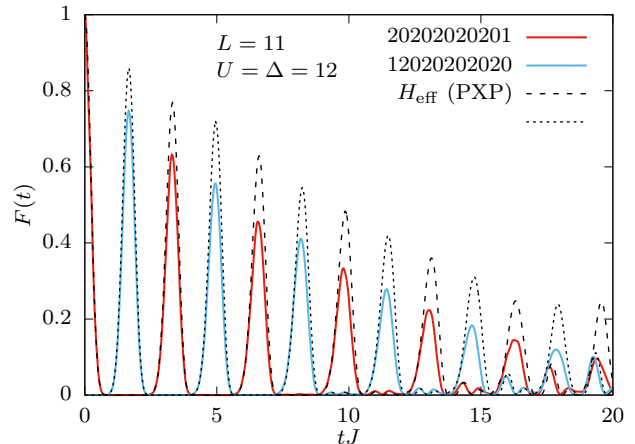


Figure S1. Evolution of quantum fidelity  $F(t) = |\langle \psi_0 | e^{-iHt} | \psi_0 \rangle|^2$  starting from the state  $|\psi_0\rangle = |2020\dots 201\rangle$  (red) and the amplitude of state transfer,  $\mathcal{O}(t) = |\langle \psi | e^{-iHt} | \psi_0 \rangle|^2$ , with the state  $|\psi\rangle = |12020\dots 2020\rangle$  (blue). The evolution is governed by the tilted Bose-Hubbard Hamiltonian in Eq. (S1) with  $J=1$ ,  $U=\Delta=12$  and maximally 3 particles per site. The dashed and dotted black lines correspond to the effective model in Eq. (S4). System size  $L=11$ , filling factor  $\nu=1$ .

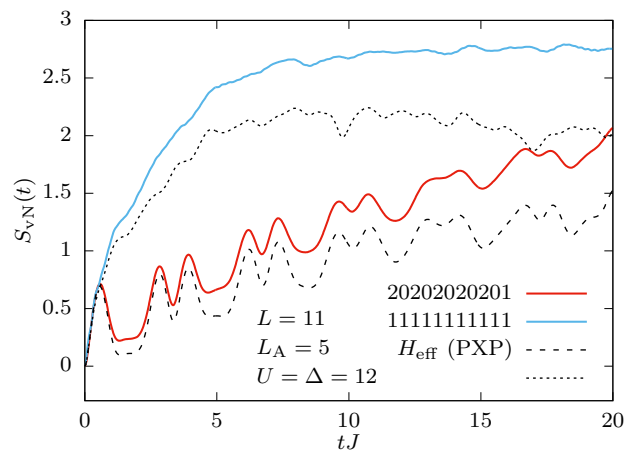


Figure S2. Evolution of the bipartite entanglement entropy for the initial states  $|2020\dots 201\rangle$  (red) and  $|111\dots 111\rangle$  (blue). The evolution is governed by the tilted Bose-Hubbard Hamiltonian from Eq. (S1) with  $J = 1$ ,  $U = \Delta = 12$  and maximally 3 particles per site. The dashed and dotted black lines correspond to the effective model from Eq. (S4). System size  $L = 11$ , subsystem  $L_A = 5$ , filling factor  $\nu = 1$ .

In Fig. S2 we show the evolution of the bipar-  
tite von Neumann entanglement entropy,  $S_{\text{vN}}(t) = -\text{Tr}_A(\hat{\rho}_A \ln \hat{\rho}_A)$ , where  $\hat{\rho}_A$  is the reduced density matrix for subsystem A of length  $L_A$ . The system is initially

1 prepared in the state 2020...201 or the completely ho- 33  
 2 mogeneous state 111...111. As in the PXP model, the 34  
 3 entanglement entropy for the 2020...201 state exhibits 35  
 4 slow and approximately linear growth in time. In con-  
 5 trast, the entanglement entropy for the state 111...111  
 6 rapidly saturates, implying that the system quickly ther-  
 7 malizes.

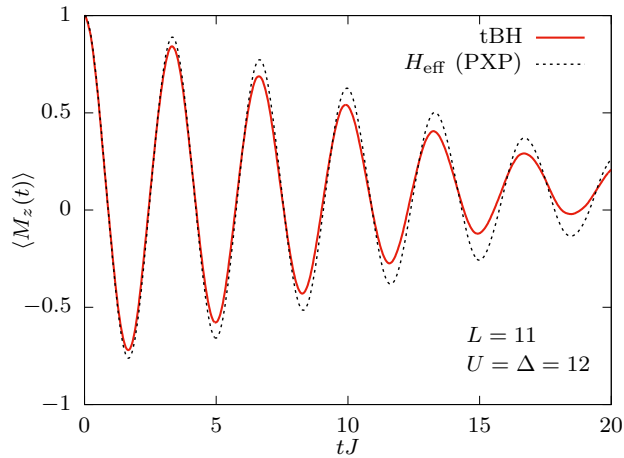


Figure S3. Evolution of staggered magnetization  $\langle \hat{M}_z \rangle = (\langle \hat{n}_{\text{odd}} \rangle - \langle \hat{n}_{\text{even}} \rangle) / (\langle \hat{n}_{\text{odd}} \rangle + \langle \hat{n}_{\text{even}} \rangle)$ , where  $\hat{n}_{\text{odd}}$  and  $\hat{n}_{\text{even}}$  are the numbers of particles on odd and even sites. The evolution is governed by the tilted Bose-Hubbard Hamiltonian from Eq. (S1) with  $J = 1$  and  $U = \Delta = 12$  (solid red line) and the effective model from Eq. (S4) which is equivalent to the PXP model (dashed black line). System size  $L = 11$ , filling factor  $\nu = 1$ , initial state  $|2020\dots 201\rangle$ .

8 The evolution of density imbalance between the even  
 9 and odd sites  $\langle \hat{M}_z \rangle = (\langle \hat{n}_{\text{odd}} \rangle - \langle \hat{n}_{\text{even}} \rangle) / (\langle \hat{n}_{\text{odd}} \rangle +$   
 10  $\langle \hat{n}_{\text{even}} \rangle)$ , which corresponds to staggered magnetization  
 11 in the PXP model, is shown in Fig. S3. This is one of the  
 12 quantities that was experimentally measured in the main  
 13 text. Here we again compare the evolution with the full  
 14 tilted Bose-Hubbard Hamiltonian (S1) and the effective  
 15 Hamiltonian (S4), the latter being equivalent to the PXP  
 16 model, and we find excellent agreement between the two.  
 17 The overlap of eigenstates in the full model in Eq. (S1)  
 18 for a chain of  $L = 9$  sites with the initial 202020201  
 19 state is given in Fig. S4. For parameter values  $U = \Delta = 12$ ,  
 20 and  $J = 1$ , the energy spectrum is split into multi-  
 21 ple bands with approximately constant expectation value  
 22 of the sum of interaction and tilt terms  $\langle \hat{H}_U + \hat{H}_\Delta \rangle$ ,  
 23 as indicated by different colors. The inset shows the  
 24 top part of the highest-overlap band (around  $E = 50$   
 25  $\langle 202020201 | \hat{H} | 202020201 \rangle = 432$ ). This band is de-  
 26 scribed by the effective Hamiltonian (S2), which pre-  
 27 serves the expectation value  $\langle \hat{H}_U + \hat{H}_\Delta \rangle$  and is equi-  
 28 valent to the PXP Hamiltonian. A band of  $L = 9$  scarred  
 29 eigenstates is visible in the inset, as expected from the  
 30 analogy with the PXP model. These scarred eigenstates  
 31 are responsible for the revival dynamics in Fig. S1. As  
 32 the two Néel states have the maximal number of dou-

blons at filling factor  $\nu = 1$ , this type of dynamics also  
 leads to oscillations in doublon number, which can be  
 experimentally measured.

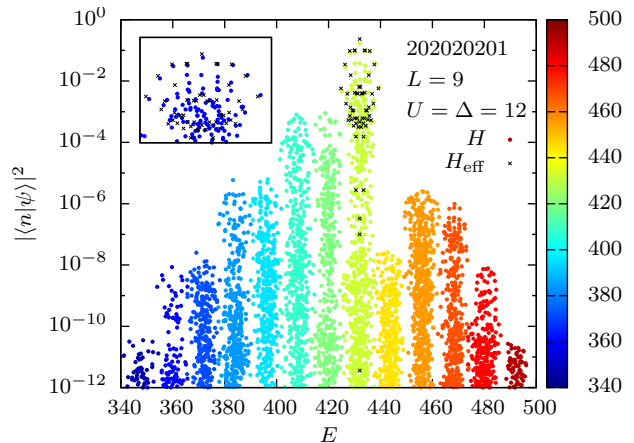


Figure S4. Overlap of the state 202020201 with the eigenstates of the tilted Bose-Hubbard model (S1) with  $J = 1$  and  $U = \Delta = 12$ . The colors indicate the expectation value of the diagonal terms  $\langle \hat{H}_U + \hat{H}_\Delta \rangle$  for each eigenstate. The black crosses correspond to the effective model (S4) (shifted by  $E = \langle 202020201 | \hat{H} | 202020201 \rangle = 432$ ). The inset shows the top part of band with the highest overlap, where a band of  $L = 9$  scarred eigenstates analogous to that in the PXP model can be seen.

As a side note, the system is also described by PXP-like effective models at other integer filling factors. The reviving initial states are of the form  $|(n+1)(n-1)(n+1)(n-1)\dots(n+1)(n-1)n\rangle$  for  $\nu = n$ , e.g.  $|3131\dots 312\rangle$  for  $\nu = 2$  and  $|4242\dots 423\rangle$  for  $\nu = 3$ , as shown in Fig. S5. Revival frequency increases with  $n$  as  $\sqrt{n(n-1)}$ , but the revivals decay faster for larger  $n$ .

## GLOBAL VS. SINGLE-SITE FIDELITY

In this section we discuss the relation between two measures of similarity of pure states used in this work. One measure is the quantum fidelity

$$\mathcal{F}(|\phi\rangle, |\psi\rangle) = \|\phi\|\psi^2, \quad (\text{S11})$$

i.e., the global overlap between two pure states. This measure is very convenient for numerical simulations and theoretical analysis, but hard to measure in experiment. For this reason, we also consider a different measure consisting of an average of local measurements:

$$\mathcal{F}_{(r)}(|\phi\rangle, |\psi\rangle) = \frac{1}{L+1-r} \sum_{j=1}^{L+1-r} \text{Tr} \left[ \hat{\rho}_{j,j+r-1}^\phi \hat{\rho}_{j,j+r-1}^\psi \right], \quad (\text{S12})$$

where  $1 \leq r \leq L$  is the range of the measurements and

$$\hat{\rho}_{j,j+r-1}^\phi = \text{Tr}_{\perp, j, j+r-1} [|\phi\rangle \langle \phi|] \quad (\text{S13})$$

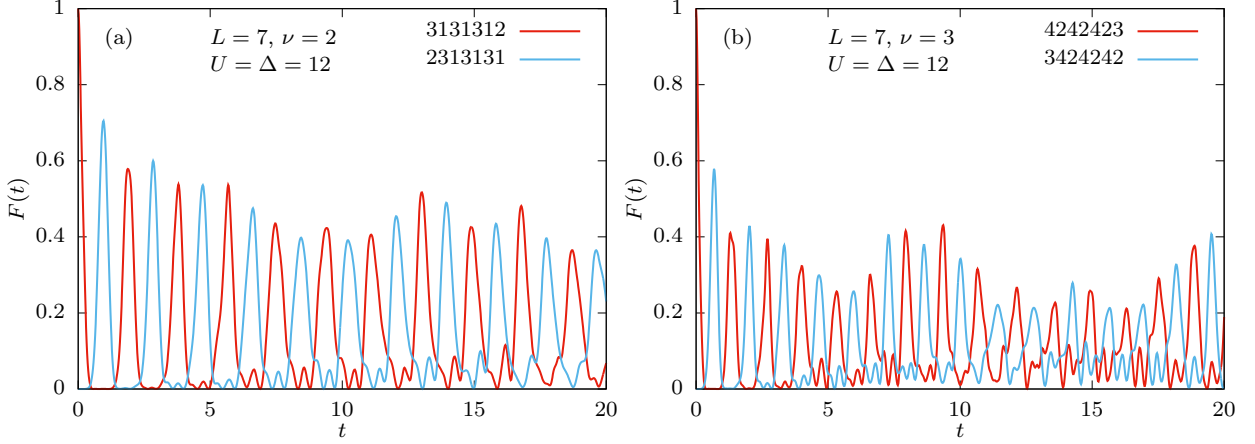


Figure S5. Evolution of quantum fidelity  $F(t) = |\langle \psi_0 | e^{-iHt} | \psi_0 \rangle|^2$  starting from the Néel state  $|\psi_0\rangle$  (red) and the amplitude of state transfer,  $\mathcal{O}(t) = |\langle \psi | e^{-iHt} | \psi_0 \rangle|^2$ , for the anti-Néel state  $|\psi\rangle$  (blue). The evolution is governed by the tilted Bose-Hubbard Hamiltonian from Eq. (S1) with  $J = 1$  and  $U = \Delta = 12$ . (a) Filling factor  $\nu = 2$ . (b)  $\nu = 3$ . The Hilbert space size is reduced by removing the configurations with more than 3 particles per site in (a) and more than 4 particles per site in (b).

1 is the density matrix obtained by performing the partial 20  
2 trace on all sites except sites  $j$  to  $j - 1 + r$ .

3 Both quantities,  $\mathcal{F}$  and  $\mathcal{F}_{(r)}$ , are real and obey

$$0 \leq \mathcal{F}(|\phi\rangle, |\psi\rangle), \mathcal{F}_{(r)}(|\phi\rangle, |\psi\rangle) \leq 1, \quad (\text{S14})$$

4 and

$$\mathcal{F}_{(r)}(|\phi\rangle, |\psi\rangle) = \mathcal{F}_{(r)}(|\psi\rangle, |\phi\rangle), \quad (\text{S15})$$

$$\mathcal{F}(|\phi\rangle, |\psi\rangle) = \mathcal{F}(|\psi\rangle, |\phi\rangle). \quad (\text{S16})$$

5 It is also important to note that

$$\begin{aligned} \mathcal{F}_{(L)}(|\phi\rangle, |\psi\rangle) &= \text{Tr} [|\phi\rangle \langle \phi | \psi\rangle \langle \psi |] \\ &= \|\phi\| \psi^2 = \mathcal{F}(|\phi\rangle, |\psi\rangle). \end{aligned} \quad (\text{S17})$$

6 While for arbitrary states  $\mathcal{F}_{(r)}$  is neither an upper bound  
7 nor a lower bound of  $\mathcal{F}$ , it does not mean that this is  
8 never the case. We are now limiting our study to the case  
9 where the state  $\phi$  is a product state. The consequence  
10 of that is that the reduced density matrix  $\hat{\rho}_{j,j+r-1}^\phi$  will  
11 correspond to a pure state for any  $r$ . We can then chose a  
12 basis for each site such that  $|\phi\rangle$  is a product of local basis  
13 states, and so a Fock basis state for the whole Hilbert  
14 space. Let us then denote the orthonormal states of this  
15 basis by  $|\alpha\rangle$ .

16 This allows us to rewrite the reduced density matrix  
17 as  $\hat{\rho}_{j,j+r-1}^\phi = |\phi_{j,j+r-1}\rangle \langle \phi_{j,j+r-1}|$ , where  $|\phi_{j,j+r-1}\rangle$  cor-  
18 responds to the state  $\phi$  for sites  $j$  to  $j + r - 1$  (remember  
19 that we can only do this because  $|\phi\rangle$  is a product state).

This formulation implies the following simplification

$$\begin{aligned} \mathcal{F}_{(r)}(|\phi\rangle, |\psi\rangle) &= \frac{1}{L+1-r} \sum_{j=1}^{L+1-r} \text{Tr} \left[ \hat{\rho}_{j,j+r-1}^\phi \hat{\rho}_{j,j+r-1}^\psi \right] \\ &= \frac{1}{L+1-r} \sum_{j=1}^{L+1-r} \text{Tr} \left[ |\phi_{j,j+r-1}\rangle \langle \phi_{j,j+r-1}| \hat{\rho}_{j,j+r-1}^\psi \right] \\ &= \frac{1}{L+1-r} \sum_{j=1}^{L+1-r} \sum_{\substack{|\alpha\rangle \text{ s.t.} \\ \langle \alpha | \phi \rangle_{j,j+r-1} = 1}} \|\alpha\| \psi^2 \\ &= \frac{1}{L+1-r} \sum_{|\alpha\rangle} \|\alpha\| \psi^2 \sum_{j=1}^{L+1-r} \prod_{k=j}^{j+r-1} \langle \alpha_k | \phi_k \rangle \\ &= \|\phi\| \psi^2 + \frac{1}{L+1-r} \sum_{|\alpha\rangle \neq |\phi\rangle} \|\alpha\| \psi^2 \sum_{j=1}^{L+1-r} \prod_{k=j}^{j+r-1} \langle \alpha_k | \phi_k \rangle \\ &\geq \|\phi\| \psi^2 = \mathcal{F}(|\phi\rangle, |\psi\rangle), \end{aligned} \quad (\text{S18})$$

21 where  $\langle \alpha | \phi \rangle_{j,j+r-1}$  denotes the product of  $\langle \alpha_{j,j+1-r} \rangle$   
22 and  $\langle \phi_{j,j+1-r} \rangle$ , which is always either 0 or 1. This means  
23 that  $\|\alpha\| \psi^2$  contributes to  $\mathcal{F}_{(r)}(|\phi\rangle, |\psi\rangle)$  with a weight  
24 of  $\frac{1}{N+1-r}$  each time  $r$  consecutive sites are in the same  
25 state in  $|\alpha\rangle$  and  $|\phi\rangle$ . This simple rule allows us to not  
26 only derive this inequality between  $\mathcal{F}$  and  $\mathcal{F}_{(r)}$ , but also  
27 to compare the effect of  $r$  on  $\mathcal{F}_{(r)}$ . Indeed, if with  $r$  a  
28 basis state  $|\alpha\rangle$  has a weight of  $\frac{n}{L+1-r}$ , then if  $n > 0$  with  
29  $r - 1$  it has a minimum weight of  $\frac{n+1}{L+2-r}$ . As  $n \leq L+1-r$ ,  
30 it implies that  $\frac{n}{L+1-r} \leq \frac{n+1}{L+2-r}$ . If  $n = 0$  then for  $r - 1$   
31 the same state cannot contribute less, and so for any  $n$   
32 it contributes more or the same amount. Hence we can  
33 conclude that

$$\mathcal{F}_{(1)}(|\phi\rangle, |\psi\rangle) \geq \mathcal{F}_{(2)}(|\phi\rangle, |\psi\rangle) \geq \dots \mathcal{F}_{(L)}(|\phi\rangle, |\psi\rangle) = \mathcal{F}(|\phi\rangle, |\psi\rangle). \quad (\text{S19})$$

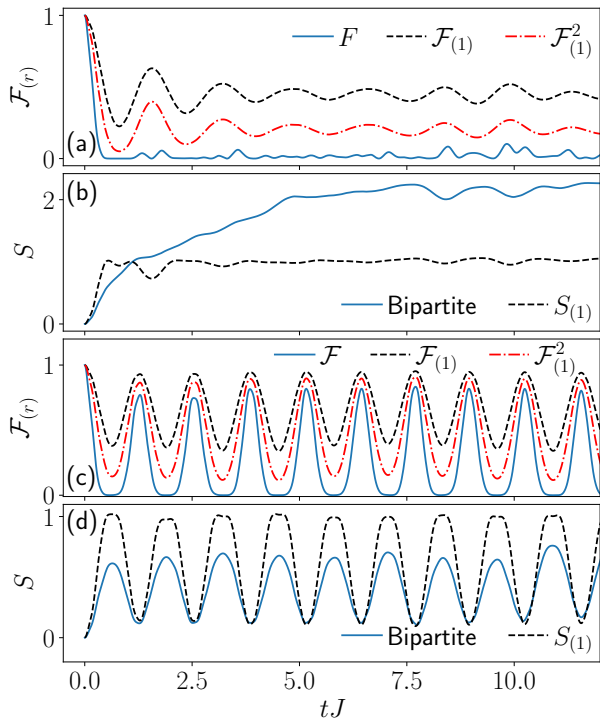


Figure S6. Comparison between global and local quantities for the polarized state (a)-(b) without and (c)-(d) with driving. Both the single-site fidelity and the single-site entropy effectively capture the behavior of their global counterpart. In both the undriven and driven cases, the squared single-site fidelity  $\mathcal{F}_{(1)}^2$  provides a better approximation of  $\mathcal{F}$  than  $\mathcal{F}_{(1)}$  while still acting as an upper bound. Tilted Bose-Hubbard model (S1),  $J = 1$ ,  $\Delta = U = 16$ ,  $L = 11$ ,  $L_A = 5$ , driving parameters  $U_0 = -2.38$ ,  $U_m = 1.54$ ,  $\omega = 4.90$ .

Finally, it is important to note that the inequality  $\frac{n}{L+1-r} \leq \frac{n+1}{L+2-r}$  is saturated if and only if  $n = L + 1 - r$ , meaning that  $|\alpha\rangle$  and  $|\phi\rangle$  are the same. This is important as  $\mathcal{F}_{(r)}(|\phi\rangle, |\psi\rangle)$  is a weighted sum of all the  $\|\alpha\|\psi^2$  with weights equal or smaller to 1. In order for  $\mathcal{F}_{(r)}(|\phi\rangle, |\psi\rangle)$  to be equal to  $\mathcal{F}_{(r-1)}(|\phi\rangle, |\psi\rangle)$ , all weights corresponding to a non-zero  $|\langle\alpha|\psi\rangle|^2$  must stay the same. But the only weights that are not increasing are either the ones that stay equal to zero or the one of  $|\alpha\rangle = |\phi\rangle$  which stays equal to one. This implies that *all* inequalities of Eq. S19 are simultaneously saturated if and only if  $|\psi\rangle = |\phi\rangle$  (in which case they are all equal to one) or  $\mathcal{F}_{(1)}(|\phi\rangle, |\psi\rangle) = 0$  (in that case they are all equal to 0). It is also possible for some of them to be saturated. This can only happen if any consecutive subset of length  $m$  of  $|\phi\rangle$  and  $|\psi\rangle$  are orthogonal, meaning the all  $\mathcal{F}_{(r)}$  are equal to 0 for all  $r \geq m$ .

In the experimental setup we only have access to the single-site fidelity  $\mathcal{F}_{(1)}$ , which already mimics the behavior of the real fidelity  $\mathcal{F}$  (see Fig. S6). While it bounds  $\mathcal{F}$  from above, that bound is fairly loose. If we instead look at its square  $\mathcal{F}_{(1)}^2$ , we can see that it approximates  $\mathcal{F}$

much better as it takes a lower value when  $\mathcal{F}$  is close to zero. While  $\mathcal{F}_{(1)}^2$  is not guaranteed to be an upper bound of  $\mathcal{F}$ , our theoretical simulations indicate that it still effectively acts as one for the conditions we study. Our simulations also show that the single-site second Renyi entropy  $S_{(1)}$  shows a very similar behavior to the bipartite half-chain second Renyi entropy  $S$ . While it is limited in the range of values it can take,  $S_{(1)}$  is clearly able to distinguish between the two regimes we are seeing in our setup: rapid entropy growth until a plateau is reached, and very slow entropy growth with oscillations on top.

### ALTERNATIVE MAPPING BETWEEN PXP AND TILTED 1D BOSE-HUBBARD WITH STAGGERED DETUNING

There is another mapping between the tilted 1D Bose-Hubbard and the PXP model which is based on the additional staggered potential term added to the the model in Eq. (S1):

$$\hat{H} = -J \sum_{i=1}^{L-1} (\hat{b}_i^\dagger \hat{b}_{i+1} + \hat{b}_{i+1}^\dagger \hat{b}_i) + \frac{U}{2} \sum_{i=1}^L \hat{n}_i (\hat{n}_i - 1) + \Delta \sum_{i=1}^L i \hat{n}_i + \frac{\delta}{2} \sum_{i=1}^L (-1)^{i-1} \hat{n}_i. \quad (\text{S20})$$

The parameter  $\delta$  determines the energy offset between even and odd lattice sites. The odd ones are now “plus” sites where the  $\delta$  term is positive, while the even one are “minus” sites where it is negative. This means that for an odd chain of length  $L$  there are  $N = \frac{L-1}{2}$  minus sites and  $N + 1 = \frac{L+1}{2}$  plus sites.

The model in Eq. (S20) has been experimentally studied (see [S10] and references therein). Its mapping to the U(1) quantum link model has been already established in the literature, as is the mapping between the U(1) quantum link model and the PXP model [S11]. However, the equivalence of the tilted Bose-Hubbard model with staggered detuning and the PXP model was to our knowledge never explicitly stated, so we will briefly explain it here. This mapping is valid in the regime  $U \approx 2\delta \gg J$  and at filling factor  $\nu = 1/2$ .

When  $U \approx 2\delta \gg J$ , the second-order process  $101 \leftrightarrow 020$  becomes resonant. Nonzero tilt  $\Delta$  makes other relevant second-order processes such as  $100 \leftrightarrow 001$  off-resonant. In this regime and for odd system size  $L$  with filling factor  $\nu = \frac{L+1}{2L}$ , the effective Hamiltonian at second order of the model in Eq. (S20) is fragmented. One of these fragments can be mapped to the PXP model up to some diagonal boundary terms. To find the corresponding state in PXP, one only needs to look at the “minus” sites. Doubtons on these sites are mapped to PXP excitations, as the resonant processes cannot create two doubtons on two adjacent minus sites. Due to

1 the nature of the resonant process they can never be  
 2 singly-occupied, and empty minus sites are mapped to  
 3 non-excited atoms. This means that the corresponding  
 4 PXP model has length  $N = \frac{L-1}{2}$ , which is just the num-  
 5 ber of minus sites.

6 The Néel states  $\bullet\circ\bullet\circ\dots\circ\bullet$  and  $\circ\bullet\circ\bullet\dots\circ\bullet$  are then  
 7 mapped to  $02000200\dots02001$  and  $100200020\dots0020$  re-  
 8 spectively, while  $101010\dots101$  corresponds to the fully  
 9 polarized state  $\circ\circ\circ\dots\circ\circ\circ$ .

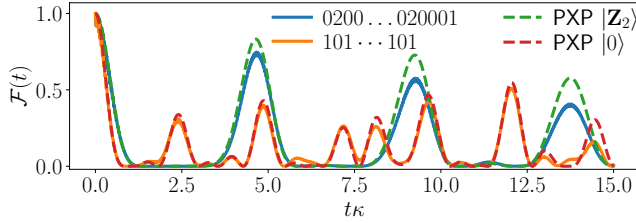


Figure S7. Time evolution of the fidelity for tilted Bose-Hubbard model with staggered detuning with  $L = 13$ ,  $U = 2\delta = 120$ ,  $J = 1$  and  $\Delta = 43.3$ , and for the PXP model with  $N = 6$ . The constant  $\kappa$  is the effective hopping strength in each model (see text).

10 Fig. S7 shows the wave function fidelity over time for  
 11 the model in Eq. (S20) with  $U=2\delta > \Delta \gg J$ , and for  
 12 the PXP model it can be mapped to. To directly compare  
 13 the two models, we have rescaled the time axis  
 14 by the constant  $\kappa$ , which takes the value  $\sqrt{2}J^{(2)} =$   
 15  $\sqrt{2} \times 4J^2U/(U^2-4\Delta^2)$  in the Bose-Hubbard model and  $\Omega$   
 16 in the PXP model. The staggered Bose-Hubbard model  
 17 oscillates between two product states,  $02000200\dots02001$   
 18 and  $100200020\dots0020$ , which are the analogs of the Néel  
 19 states in the PXP model. Overall, the dynamics is seen  
 20 to be very similar in the two models, with the slight differ-  
 21 ence between the two being likely due to the boundary  
 22 terms defined in Eq. (S21) below.

23 To derive the mapping to the PXP model rigorously,  
 24 we can separate the Hamiltonian in Eq. (S20) as  $\hat{H} =$   
 25  $\hat{H}_0 - J\hat{V}$  and perform the Schrieffer-Wolff transformation  
 26 [S7]. Here  $\hat{H}_0$  encompasses all the diagonal terms while  
 27  $\hat{V}$  simply corresponds to hopping, which assumes that  
 28  $\delta, \Delta, U \gg J$ . Furthermore, we will only focus on the  
 29 regime  $U = 2\delta$ , in which case there are no first order  
 30 terms. If  $U$  is close but not equal to  $2\delta$ , then the effective  
 31 Hamiltonian at first order will contain diagonal terms  
 32 proportional to  $|U - 2\delta|$ . Finally, we only focus on the  
 33 connected component of the second order Hamiltonian  
 34 that can be mapped to the PXP model, meaning that  
 35 resonant processes like  $02010 \leftrightarrow 11001$  are ignored as  
 36 these configuration cannot appear in the Hilbert space  
 37 component of interest.

38 In the relevant part of the Hilbert space, the only off-  
 39 diagonal resonant process at second order is  $101 \leftrightarrow 020$ ,  
 40 which appears with a weight of  $\sqrt{2}J^{(2)}$ , where  $J^{(2)} =$

$\frac{4J^2U}{U^2-4\Delta^2}$ . There are also two allowed second-order di-  
 agonal processes in the bulk of the chain:  $010 \leftrightarrow 010$   
 and  $020 \leftrightarrow 020$ . They have a respective weight of  $J^{(2)}$   
 and  $2J^{(2)}$ . However, as creating a new doublon means  
 emptying two singly-occupied sites, the diagonal matrix  
 elements do not change under the off-diagonal process.  
 The only exception to this is hopping at the boundaries  
 of the chain. For the leftmost site, only hopping to the  
 right and then back is possible, leading to a contribution  
 of  $\frac{2J^2}{U-2\Delta}$  instead of  $J^{(2)}$ . For the rightmost site only hop-  
 ping to the left is possible and the contribution is  $\frac{2J^2}{U+2\Delta}$ .  
 This means that not all diagonal matrix elements are  
 the same but they vary between  $J^{(2)}N = \frac{L-1}{2}J^{(2)}$  and  
 $(N+1)J^{(2)} = \frac{L+1}{2}J^{(2)}$ . However the differences between  
 the diagonal elements are  $\mathcal{O}(1)$  and do not scale with  $L$ ,  
 so they become negligible for large system sizes. All to-  
 gether, the second order Hamiltonian can be mapped to  
 the following model.

$$\hat{H}_{\text{eff},2} = J^{(2)}N + \sqrt{2}J^{(2)} \left[ \hat{X}_1 \hat{P}_2 + \hat{P}_{N-1} \hat{X}_N \right. \\ \left. + \sum_{j=2}^{N-1} \hat{P}_{j-1} \hat{X}_j \hat{P}_{j+1} \right] + \frac{2J^2}{U+2\Delta} \hat{n}_1 + \frac{2J^2}{U-2\Delta} \hat{n}_N, \quad (\text{S21})$$

with  $J^{(2)} = \frac{4J^2U}{U^2-4\Delta^2}$ ,  $N = \frac{L-1}{2}$ ,  $\hat{n}_j = \frac{1+Z_j}{2}$ , where  $Z$   
 denotes the usual Pauli  $z$  matrix [ $\hat{P}_j$  and  $\hat{X}_j$  were de-  
 fined previously below Eq. (S5)]. It is worth mentioning  
 that for  $U = 2\delta$ , the third order effective Hamiltonian is  
 identically zero due to the absence of diagonal elements  
 in the perturbation  $V$  (which is simply the hopping) and  
 the next correction only happens at fourth order.

## EFFECT OF PERIODIC DRIVING ON $\mathbb{Z}_2$ SCARS

In this section we numerically explore the effect of driv-  
 ing on the stabilization of many-body scars and revival  
 dynamics, both in the PXP and tilted Bose-Hubbard  
 models.

### Driven PXP model

Periodic driving has been shown to enhance and sta-  
 bilize the revivals in the PXP model [S12, S13]. The  
 optimal driving frequency was found to be close to twice  
 that of revivals in the pure PXP model without driving.  
 We consider the following spatially-uniform cosine driv-  
 ing scheme which was also experimentally implemented  
 in Ref. [S12]

$$\hat{H}(t) = \sum_i \left( \Omega \hat{P}_{i-1} \hat{X}_i \hat{P}_{i+1} - \mu(t) \hat{n}_i \right), \quad (\text{S22})$$

$$\mu(t) = \mu_0 + \mu_m \cos(\omega t). \quad (\text{S23})$$

1 Here,  $\mu_0$  is the static detuning,  $\mu_m$  modulation amplitude and  $\omega$  driving frequency. For simplicity, when working with the PXP model, we impose periodic boundary conditions (PBC). We determine the optimal values of  $\mu_0$  and  $\mu_m$  by scanning the parameter space for the highest time-averaged fidelity. To make sure we found the globally-optimal values of the driving parameters, we have also checked the results against the simulated annealing algorithm implemented in GNU Scientific Library.

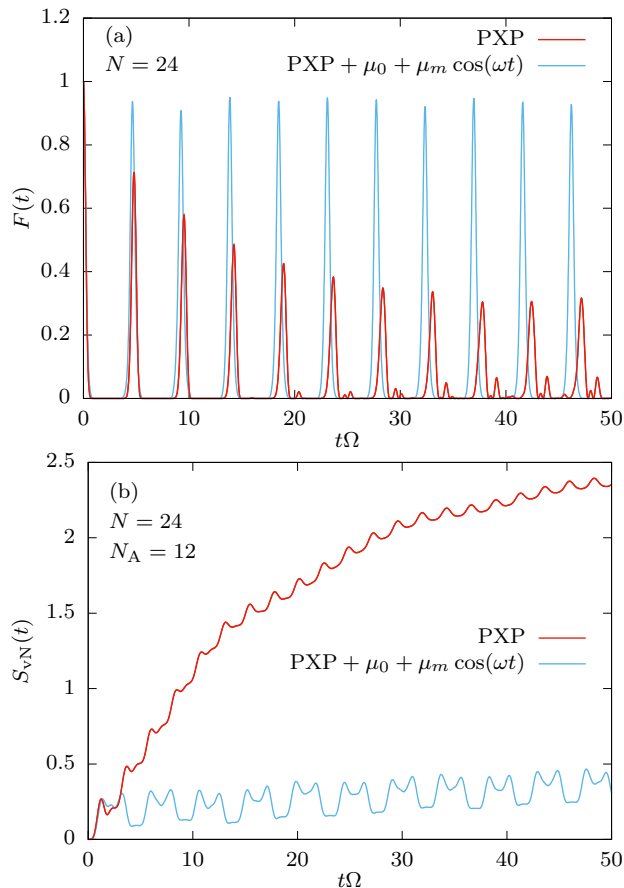


Figure S8. Comparison of dynamics in the pure (red), and periodically driven PXP model (blue). System size  $N = 24$ , driving parameters  $\mu_0/\Omega = 1.15$ ,  $\mu_m/\Omega = 2.67$ ,  $\omega/\Omega = 2.72$ . (a) Fidelity. (b) Entanglement entropy for  $N_A = 12$ .

11 The evolution of quantum fidelity starting from the  
12 Néel state  $|\mathbb{Z}_2\rangle = |\bullet\circ\bullet\circ\bullet\circ\dots\rangle$  can be seen in Fig. S8(a),  
13 both without driving (red) and driven with optimal driv-  
14 ing parameters  $\mu_0/\Omega = 1.15$ ,  $\mu_m/\Omega = 2.67$  and  $\omega/\Omega =$   
15 2.72 (blue). Driving leads to high revivals whose ampli-  
16 tude remains close to 1 over very long times. Addition-  
17 ally, the driving also strongly suppresses the growth of  
18 entanglement entropy, as can be observed in Fig. S8(b).  
19

20 In order to understand the mechanism of revival en-  
21 hancement, in Fig. S9 we show the effects of periodic  
22 driving on the trajectory in the Hilbert space. The  $x$  and  $y$  axes in this figure are the expected numbers of ex-

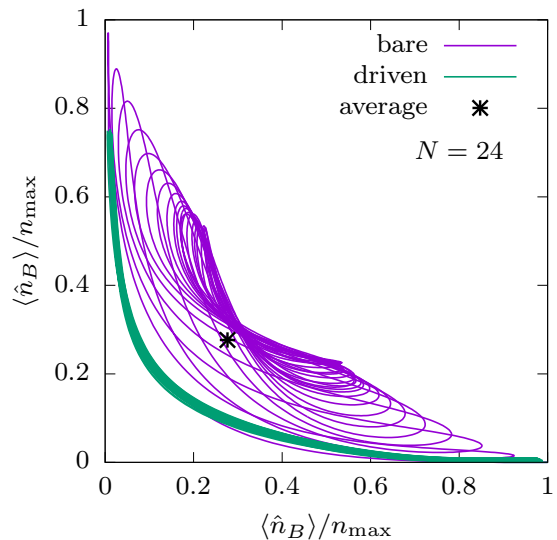


Figure S9. Trajectory in the Hilbert space, represented by the the expected numbers of excitations on the even and odd sublattices,  $\langle \hat{n}_A \rangle$  and  $\langle \hat{n}_B \rangle$ , normalized by the maximal number of excitations  $\hat{n}_{\max} = N/2$ . Purple: no driving,  $\mu(t) = 0$ . The trajectory at first keeps returning to the vicinity of the Néel states, but then slowly relaxes towards the average value of  $\langle \hat{n}_A \rangle$  and  $\langle \hat{n}_B \rangle$ . Green: driving with optimal parameters  $\mu_0/\Omega = 1.15$ ,  $\mu_m/\Omega = 2.67$  and  $\omega/\Omega = 2.72$ , results in dynamics that sharply concentrates around the trajectory and avoids thermalization.

23 citations on the even and odd sublattice (normalized by  
24 the maximal number of excitations  $n_{\max} = N/2$ ),  $\langle \hat{n}_A \rangle$   
25 and  $\langle \hat{n}_B \rangle$  respectively. The two Néel states are located  
26 in the bottom right and top left corner of Fig. S9, while  
27 the polarized state  $|\circ\circ\circ\dots\rangle$  is in the bottom left corner.  
28 The states on the main diagonal (except the Néel states)  
29 and in the triangle above it are forbidden due to the PXP  
30 constraints.

31 In the undriven case (purple), the trajectory at first os-  
32 cillates between the Néel and anti-Néel states in the cor-  
33 ners, while passing through a region with a lower number  
34 of excitations (bottom left). However, as the time pro-  
35 gresses, the wavefunction starts to thermalize and the  
36 trajectory drifts towards towards the average numbers  
37 of excitations  $(\langle \hat{n}_A \rangle, \langle \hat{n}_B \rangle) = (0.276, 0.276)$ . When the  
38 driving is turned on (green), the trajectory continues to  
39 approximately repeat the first revival period in the un-  
40 driven case and does not seem to thermalize even at very  
41 late times. In this way the revivals are stabilized and  
42 enhanced. Another effect of driving is that the overlap  
43 with the anti-Néel state is now lower, but its peaks do  
44 not decay with time.

45 Finally, in Fig. S10 we studied the Floquet modes  
46 of the driven PXP model. The Floquet modes are a  
47 generalization of eigenstates for periodic time-dependent  
48 Hamiltonians  $\hat{H}(t + \frac{2\pi}{\omega}) = \hat{H}(t)$ . Unlike the eigenstates,  
49 the Floquet modes evolve in time, but they are time-

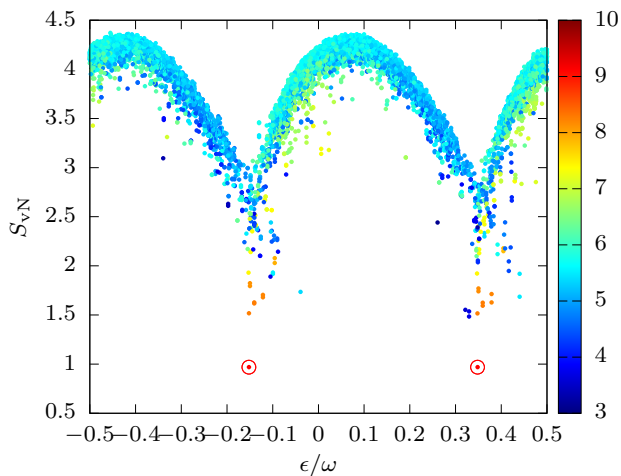


Figure S10. Bipartite von Neumann entanglement entropies of all Floquet modes for the driven PXP model with driving parameters  $\mu_0/\Omega = 1.15$ ,  $\mu_m/\Omega = 2.67$  and  $\omega/\Omega = 2.72$ . System size  $N = 20$ , subsystem  $N_A = 10$ . The colour scale represents the expectation value of the total number of excitations for each state. The two Floquet modes which have the highest overlap with the Néel state are encircled in red. They have the lowest entanglement entropy and the highest number of excitations and their quasienergies are separated by  $\omega/2$ .

1 periodic with the same periodicity as the driven Hamil-  
 2 tonian,  $\Phi_n(t + \frac{2\pi}{\omega}) = \Phi_n(t)$ . We have computed all the  
 3 Floquet modes  $\Phi_n(t=0)$  for the driven case by numerically  
 4 constructing the evolution operator over one period  
 5  $T = \frac{2\pi}{\omega}$ ,  $\hat{U}(T)$ , and diagonalizing it.

6 In Fig. S10 we plot the bipartite von Neumann entan-  
 7 glement entropies of all the Floquet modes for the opti-  
 8 mal driving parameters. There are two symmetric “arcs”  
 9 in the entropy plot, which suggests that the Floquet  
 10 Hamiltonian might be fractured into two components.  
 11 The expected numbers of excitations for each mode are  
 12 represented by different colours. The two lowest entropy  
 13 modes have the highest overlap with the Néel state  $|\mathbb{Z}_2\rangle$ .  
 14 One of them is approximately  $\Phi_1(0) = (|\mathbb{Z}_2\rangle + |\mathbb{Z}'_2\rangle)/\sqrt{2}$   
 15 and the other is close to  $\Phi_2(0) = (|\mathbb{Z}_2\rangle - |\mathbb{Z}'_2\rangle)/\sqrt{2}$ ,  
 16 while the quasienergy separation between them is  $\Delta\epsilon =$   
 17  $\epsilon_1 - \epsilon_2 \approx \omega/2$ . This provides a simple explanation for the  
 18 revival dynamics starting from the Néel state, as will be  
 19 outlined below.

Let us assume that the two idealized states  $\Phi_1(0)$  and  
 $\Phi_2(0)$  are indeed Floquet modes. The initial state  $|\mathbb{Z}_2\rangle$   
 will then be a superposition of only these two modes

$$\psi(0) = \frac{1}{\sqrt{2}}\Phi_1(0) + \frac{1}{\sqrt{2}}\Phi_2(0) \quad (\text{S24})$$

and will evolve as

$$\begin{aligned} \psi(t) &= \frac{1}{\sqrt{2}}e^{-i\epsilon_1 t}\Phi_1(t) + \frac{1}{\sqrt{2}}e^{-i\epsilon_2 t}\Phi_2(t) = \\ &= \frac{1}{\sqrt{2}}e^{-i\epsilon_1 t}(\Phi_1(t)) + e^{i\Delta\epsilon t}\Phi_2(t). \end{aligned} \quad (\text{S25})$$

After one driving period, the two Floquet modes will re-  
 turn to their initial states, but the relative phase will  
 be  $e^{i\frac{\omega}{2}\frac{2\pi}{\omega}} = e^{i\pi} = -1$ . The wavefunction after one period  
 will therefore be in the anti-Néel state (with an unim-  
 portant phase prefactor),  $\psi(T) = e^{-i\epsilon_1 T}|\mathbb{Z}'_2\rangle$ . It will take  
 two driving periods for the relative phase to again become  
 $+1$  and the wavefunction to return to the initial  $|\mathbb{Z}_2\rangle$   
 state. This is the origin of the period doubling (subhar-  
 monic response to periodic driving) which was observed  
 in previous works [S12].

We note that the period doubling will disappear if we  
 resolve the translation symmetry and work only in the  
 $k = 0$  momentum subspace. The initial state  $(|\mathbb{Z}_2\rangle +$   
 $|\mathbb{Z}'_2\rangle)/\sqrt{2}$  will in that case have high overlap with only a  
 single Floquet mode and will trivially oscillate with the  
 same frequency as the periodic drive.

### Driving the tilted 1D Bose-Hubbard model

As the tilted Bose-Hubbard model can be mapped to  
 the PXP model in the  $U \approx \Delta \gg J$  limit, see Section ,  
 we also expect to be able to enhance many-body scar-  
 ring via periodic modulation of the term corresponding  
 to the number of excitations. In the Bose-Hubbard case,  
 such a term is conveniently provided by the on-site in-  
 teraction strength  $U$ . However, we cannot use periodic  
 boundary conditions due to the linear tilt which would  
 be discontinuous at the boundary. We therefore consider  
 the Bose-Hubbard model with open boundary conditions  
 and periodically modulate the interaction strength  $U(t)$ :

$$\begin{aligned} \hat{H}(t) &= -J \sum_{i=1}^{L-1} (\hat{b}_i^\dagger \hat{b}_{i+1} + \hat{b}_{i+1}^\dagger \hat{b}_i) \\ &+ \frac{U(t)}{2} \sum_{i=1}^L \hat{n}_i (\hat{n}_i - 1) + \Delta \sum_{i=1}^L i \hat{n}_i, \end{aligned} \quad (\text{S26})$$

with the driving given by

$$U(t) = \Delta + U_0 + U_m \cos(\omega t). \quad (\text{S27})$$

The driving parameters,  $U_0$ ,  $U_m$  and  $\omega$ , are the static de-  
 tuning and the modulation amplitude of the interaction  
 strength and the driving frequency, respectively.

The modulation of interaction strength indeed leads  
 to enhanced revivals in the Bose-Hubbard model, see  
 Fig. S11. In particular, the slope of entanglement growth  
 is significantly reduced, with scarred oscillations becom-  
 ing more pronounced. However, in local observables,

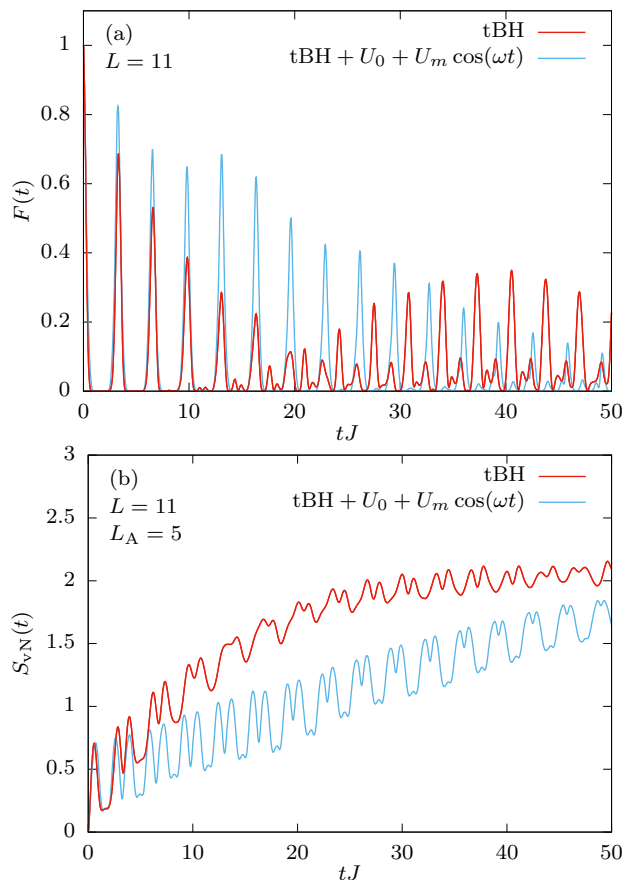


Figure S11. Comparison of the dynamics in the tilted Bose-Hubbard model without (red) and with periodic driving (blue). System size  $L = 11$ , maximally 3 particles per site,  $J = 1$ ,  $\Delta = 16$ , driving parameters  $U_0 = 1.85$ ,  $U_m = 3.71$ ,  $\omega = 3.85$ . (a) Fidelity. (b) Entanglement entropy for subsystem size  $L_A = 5$  sites.

1 such as the density of doublons, the effects of driving are  
 2 less striking than in the pure PXP model. The reason  
 3 for more modest enhancement of revivals in the Bose-  
 4 Hubbard model is the competition between stabilization  
 5 of revivals within the PXP subspace and the processes  
 6 which destroy the mapping to PXP model, such as the  
 7 terms creating 3 or more bosons on a site. Addition-  
 8 ally, the optimal driving parameters are not the same as  
 9 those for the PXP model (up to the trivial rescaling by  
 10  $\Omega = \sqrt{2}J$  to match the normalization of off-diagonal ma-  
 11 trix elements). Increasing the tilt parameter  $\Delta$  brings the  
 12 tilted Bose-Hubbard model closer to the PXP model, but  
 13 it is still necessary to perform a separate optimization of  
 14 driving parameters.

## 15 QUANTUM MANY-BODY SCARS IN THE 16 POLARIZED STATE

17 In the main text we reported the observation of many-  
 18 body scarring associated with the state that contains

19 no doublons,  $|111\dots\rangle$ , or equivalently the fully-polarized  
 20 state  $|\circ\circ\circ\dots\rangle$  in the PXP model. In this section we pro-  
 21 vide extensive theoretical evidence for many-body scarring  
 22 in the polarized state. While the polarized state does  
 23 not exhibit many-body scarring in the pure PXP model,  
 24 consistent with previous work [S14], it does display weak  
 25 signatures of non-ergodicity in local observables for suf-  
 26 ficiently small systems. In this section, we show that  
 27 static detuning and its periodic modulation can be used  
 28 to stabilize the scarring from this initial state. As we will  
 29 demonstrate below, the many-body scarring in the polar-  
 30 ized state is distinct from the previously studied “dynamical  
 31 freezing” regime associated with  $|\circ\circ\circ\dots\rangle$  state in  
 32 the PXP model driven by a square pulse protocol [S15].

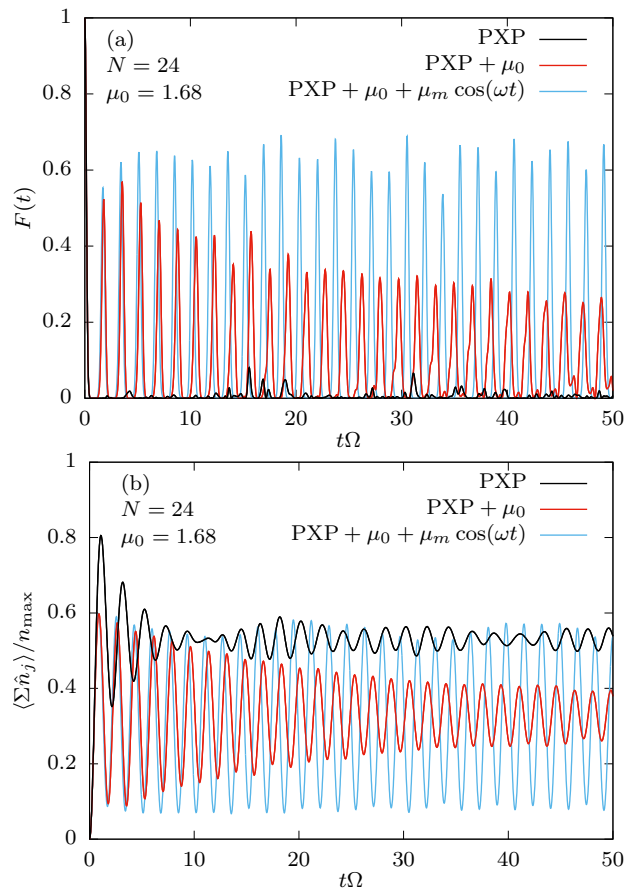


Figure S12. Comparison of dynamics from the polarized state in the pure PXP model (black), with static detuning only (red), and with both static detuning and periodic driving (blue). System size  $N = 24$ , driving parameters  $\mu_0/\Omega = 1.68$ ,  $\mu_m/\Omega = -0.50$ ,  $\omega/\Omega = 3.71$ . (a) Fidelity. (b) Expected total number of excitations normalized by the maximal number of excitations  $n_{\max} = N/2$ .

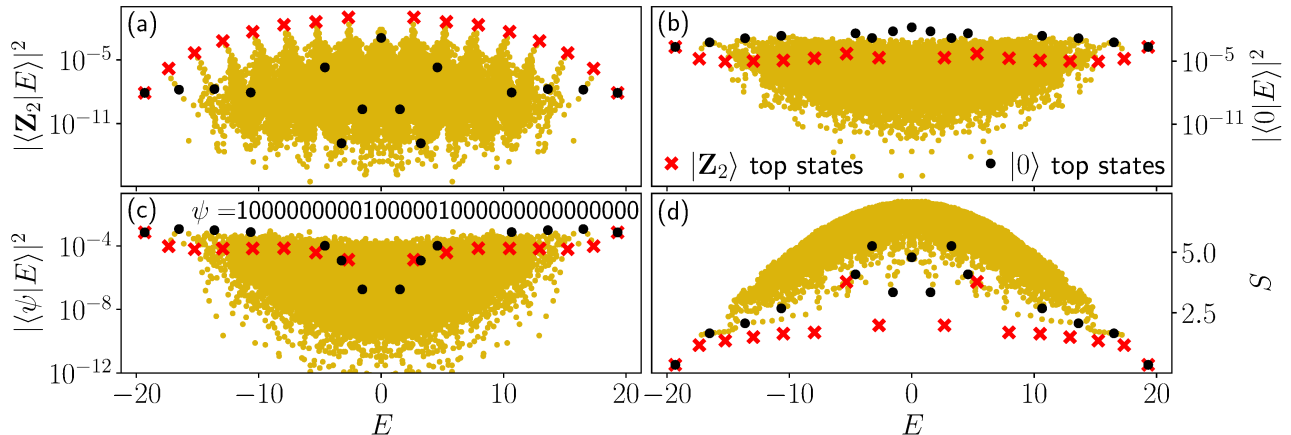


Figure S13. PXP eigenstates, system size  $N = 32$ , symmetry sector  $\{k = 0, p = 1\}$ . Overlap with (a) Néel state. (b) polarized state. (c) randomly chosen state. (d) Bipartite entanglement entropies of all eigenstates. The highest-overlap eigenstates in their energy window are marked by red crosses for the Néel state and by black dots for the polarized state.

### Pure PXP model

The polarized state  $|\circ\circ\circ\dots\rangle$  is expected to thermalize in the pure PXP model. Nevertheless, the state exhibits some signatures of non-ergodic dynamics in smaller system sizes, such as oscillations in the expectation values of certain local observables. For example, as shown by the black lines in Figs. S12(a) and (b), even though there are no significant revivals in wave function fidelity, some oscillations in the number of excitations are still visible.

A closer look at the eigenstates of the PXP Hamiltonian and their overlap with the polarized state reveals the underlying reason for this behaviour, see Fig. S13. In Fig. S13(a) we plot the overlap of all PXP eigenstates with the Néel state, showing the well known band [S5] of scarred eigenstates marked by the red crosses and corresponding tower structures. In contrast, there is no such band of high-overlap eigenstates for a randomly chosen state, see Fig. S13(c). The polarized state is between these two cases, as can be observed in Fig. S13(b). Although there is no well defined band of scarred eigenstates as for the Néel state, there is still a number of unusually high-overlap eigenstates which are marked by the black dots. Finally, in Fig. S13(d) we show the entanglement entropies of all eigenstates. The lowest-entropy eigenstates are the Néel state scars (red crosses), but the eigenstates with the highest overlap with the polarized state (black dots) also have lower than average entanglement entropies. Thus, we conclude that the polarized state is poised to develop many-body scarring by a suitable perturbation of the PXP model. We next show that this can be achieved by applying static detuning.

### Static detuning in the PXP model

The addition of a static detuning term

$$\hat{H}(\mu_0) = \hat{H}_{\text{PXP}} + \mu_0 \sum_j \hat{n}_j \quad (\text{S28})$$

results in the appearance of a band of atypical eigenstates with high overlap with the polarized state, as can be observed in Fig. S14. The band is still not well separated from the bulk at lower values of  $\mu_0/\Omega$ , see Figs. S14(a) and (b). At larger values of  $\mu_0/\Omega$ , the energy spectrum starts to split into disconnected bands, as shown in Fig. S14(d). We are interested in the intermediate regime shown in Fig. S14(c),  $\mu_0/\Omega \approx 1.68$ , where there is a clearly visible band of scarred states, but the bulk of the energy spectrum is still continuous.

In addition to having the highest overlap with the polarized state, the special states are also approximately equidistant in energy and have lower entanglement entropy than most other eigenstates. These are all paradigmatic properties of quantum many-body scars. However, one striking difference compared to the Néel state scars is that the highest-overlap states are not concentrated in the middle of the spectrum. Instead, most of them are located at one edge of the energy spectrum, but the band of atypical states still continues well into the higher energy densities, see Fig. S14(c). The fact that special eigenstates are biased towards one end of the spectrum is expected since the detuning potential breaks the particle-hole symmetry of the PXP Hamiltonian [S6].

This emergence of scarred eigenstates significantly affects the revival dynamics, as illustrated in Figs. S12 and S15. For the Néel state in Fig. S15(a), the detuning monotonically destroys the revival, until we reach the regime of very large detuning  $\mu_0 \gtrsim 3$  which places the Néel state in its own fragment of the Hilbert space. By

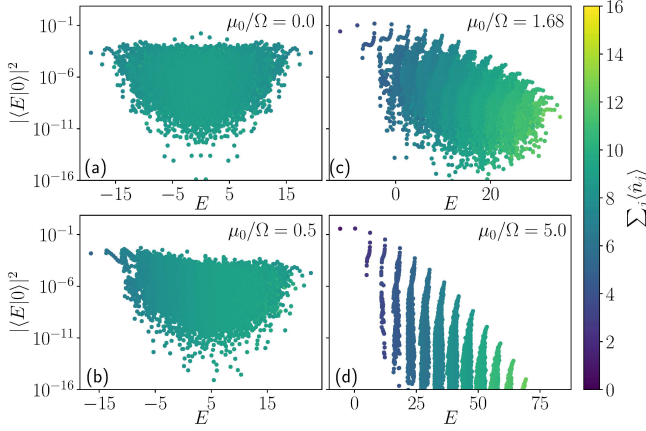


Figure S14. Overlap between the polarised state and the PXP eigenstates in the symmetry sector  $\{k = 0, p = 1\}$  for  $N = 32$ . Each subfigure corresponds to a different value of the static detuning, and the color indicates the expectation value of the number of excitations for each eigenstate.

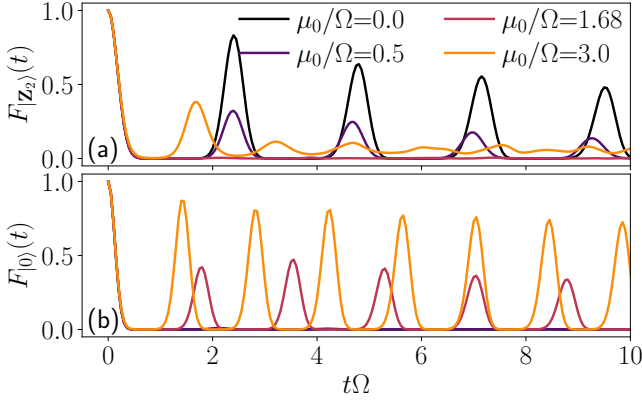


Figure S15. Revival fidelity for the Néel and polarised states in the symmetry sector  $\{k = 0, p = 1\}$  for  $N = 32$ . (a) Néel state. (b) polarized state. At low detuning only the Néel states revives while in for  $\mu_0/\Omega \gg 1$  both states do. However in the intermediate regime  $\mu_0/\Omega \approx 1$  only the polarised states has revivals while the Néel state thermalises like the other product states.

1 contrast, for the polarized state in Fig. S15(b) we see the 30  
 2 revivals start to emerge at moderate detuning  $\mu_0/\Omega \approx 1$ . 31  
 3 The frequency of the revival is found to match the energy 32  
 4 separation between the scarred states in Fig. S14(c). 33  
 5 The oscillations in the number of excitations are also en- 34  
 6 hanced and their frequency has changed to the frequency 35  
 7 of fidelity revivals. This is the regime that corresponds 36  
 8 to the many-body scarring observed in experiment. We  
 9 note that the revivals from the polarized state also per-  
 10 sist in the trivial large-detuning limit ( $\mu_0 \gtrsim 3$ ) where the 37  
 11 polarized state is effectively in its own fragment of the  
 12 Hilbert space, similar to the Néel state. 38  
 13 The addition of detuning not only affects the short- 39

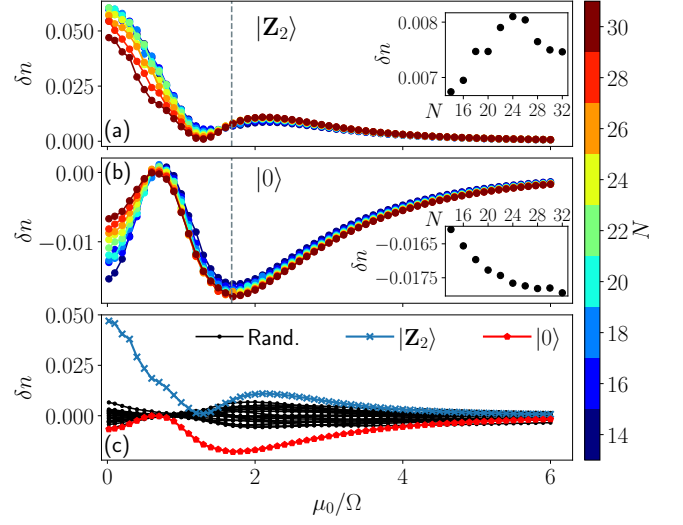


Figure S16. Difference of expectation value between the diagonal and canonical ensemble for the operator  $\frac{1}{N} \sum_j \hat{n}_j$  in the PXP model. (a) Néel state. (b) polarized state. (c) comparison of different states for  $N = 30$ . The color scale in (a) and (b) corresponds to the system size  $N$ , while the insets show the results for various  $N$  with  $\mu_0/\Omega$  fixed to 1.68 (along the grey dashed line).

14 time dynamics, but also *infinite-time* expectation val-  
 15 ues. After a quench, the value of any observable will  
 16 reach the value predicted by the diagonal ensemble  
 17  $O_d = \sum_{i,j} O_{i,j} \delta_{i,j} c_j c_i^*$ , where  $O_{i,j} = \langle E_i | O | E_j \rangle$   
 18 and  $c_i = \langle E_i | 0 \rangle$ . However we also expect the observable to  
 19 thermalize towards the value predicted by the canonical  
 20 ensemble  $O_{th} = \text{Tr} [\hat{\rho}_{th} \hat{O}]$ , where  $\hat{\rho}_{th} = \frac{1}{\mathcal{Z}} e^{-\beta \hat{H}}$  with  
 21  $\mathcal{Z} = \text{Tr} [e^{-\beta \hat{H}}]$  and  $\beta$  the inverse temperature. Note  
 22 that we also restrict  $\hat{H}$  to the symmetry sector invari-  
 23 ant under translation and spatial inversion as it is the  
 24 only one compatible with the  $|0\rangle$  state. A large differ-  
 25 ence between the predictions of these two ensembles for  
 26 a given initial state is an indicator of the violation of the  
 27 Eigenstate Thermalization Hypothesis [S16, S17]. For  
 28 the PXP model we will use the operator  $\hat{n} = \frac{1}{N} \sum_j \hat{n}_j$ ,  
 29 which counts the average number of excitations in the  
 30 system [S18], and denote the difference between the en-  
 31 semble predictions by  $\delta n$ . The Néel state is most ather-  
 32 mal at zero detuning, while the peak for the polarised  
 33 state occurs around  $\mu_0/\Omega = 1.7$ , see Fig. S16. For larger  
 34 values of the detuning these two states become respec-  
 35 tively the topmost and ground states, meaning that the  
 36 temperature is  $\pm\infty$  and both ensembles agree exactly.

### Periodic driving in the PXP model

Finally, in order to stabilize revival and many-body  
 scarring in the polarized state at *late* times, we need

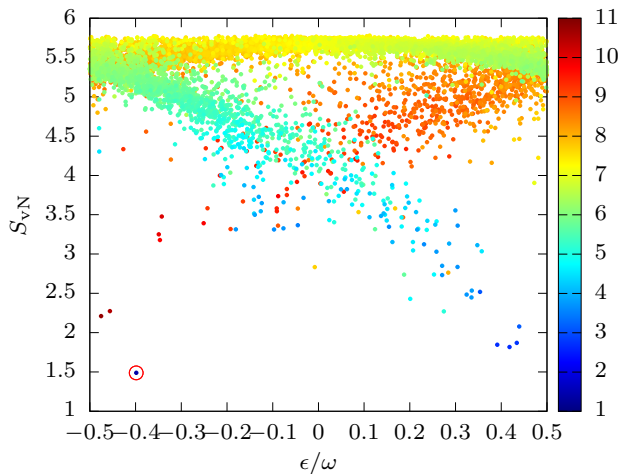


Figure S17. Bipartite von Neumann entanglement entropies of all Floquet modes for  $\mu_0/\Omega = 1.68$ ,  $\mu_m/\Omega = -0.50$  and  $\omega/\Omega = 3.71$ . System size  $N = 26$ , subsystem  $N_A = 13$ , symmetry sector  $k = 0$ . The colour scale represents the expectation value of the total number of excitations for each state. The Floquet mode with the highest overlap with the polarized state is encircled in red. This mode has the lowest entanglement entropy and the lowest number of excitations.

to modulate the detuning amplitude, in addition to the static detuning. Using the same driving protocol as for the Néel state in Eq. (S23), we can enhance and stabilize the revivals from the polarized state at late times – see Fig. S12 (blue lines). The optimal driving frequency is found to be close to the frequency of revivals in the undriven case with static detuning.

In Fig. S17 we plot the entanglement energies of all the Floquet modes  $\Phi_n(t = 0)$  for the optimal driving parameters. As in Fig. S10, the colour scale represents the expected number of excitations for each mode. The translational symmetry is now resolved and we show only the modes inside the  $k = 0$  momentum subspace. There is a single mode that has high overlap with the polarized state, which explains the revival dynamics in Figs. S12 and S15(b). Note that there is no period doubling in this case.

### Detuning and periodic driving in the tilted Bose-Hubbard model

Finally, we confirm that our conclusions about many-body scarring associated with the polarized state also hold in the full tilted Bose-Hubbard model in the regime  $U \approx \Delta$ , where we expect the effective description to be close to the PXP model. We will show that the driving leads to a strong suppression of entanglement growth and makes off-resonant the processes that cause leakage out of the PXP subspace.

In Fig. S18 we compare the dynamics at the reso-

nance  $U = \Delta$  (black lines, corresponding to the pure PXP model), at  $U = \Delta + U_0$  (red lines, corresponding to the PXP model with static detuning), and for  $U(t) = \Delta + U_0 + U_m \cos(\omega t)$  (blue lines, corresponding to the periodically driven PXP model). Due to the very fast growth of the Hilbert space size, we restrict the maximal number of bosons per site to 3. The results are consistent with those for the PXP model shown in Fig. S12. Note that the frequency of fidelity revivals in Fig. S18(a) is the frequency of PXP revivals multiplied by a factor of  $\sqrt{2}$  which comes from the off-diagonal matrix elements in the Bose-Hubbard model. The expected number of doublons, which is related to the number of PXP excitations is shown in Fig. S18(b).

The growth of entanglement entropy is suppressed by the addition of static detuning and even more by periodic driving, see Fig. S18(c). There are two factors that contribute to this behaviour. One is the dynamics inside the PXP subspace. The other is related to the leakage out of this subspace, which is represented by the number of sites with 3 particles in Fig. S18(d). The static detuning by itself significantly decreases this quantity, while the periodic driving does not seem to result in a substantial further improvement for the polarized state.

### OTHER QUANTUM MANY-BODY SCARRED STATES

In addition to the Néel state and the polarized state, we also find other initial states which revive in the PXP model with static detuning, Eq. (S28). These initial states are the ground states of  $\hat{H}(\mu_i)$  and they exhibit revivals when the detuning is quenched to a different value,  $\hat{H}(\mu_i) \rightarrow \hat{H}(\mu_f)$ . This setup generalizes the quench protocols studied in the main text. For example, setting  $\mu_i \rightarrow -\infty$ , the ground state is simply the Néel state and then quenching to  $\mu_f=0$  (pure PXP model) leads to the appearance of  $\mathbb{Z}_2$  quantum many-body scars. Similarly, if we set  $\mu_i \rightarrow \infty$  then the ground state is the  $|0\rangle$  state and quenching to  $\mu_f=1.68\Omega$  also leads to scarring, as shown in the main text.

However, we observe similar scarring phenomenology in a larger set of initial conditions by varying the parameters  $\mu_i$  and  $\mu_f$ . Unlike the Néel state and the polarized state, the ground states of  $\hat{H}(\mu_i)$  are far from product states for  $|\mu_i| < 2$ . However, they also have low entanglement and can be prepared experimentally. In Fig. S19 we illustrate this with an example for  $\mu_i = -0.76\Omega$  and  $\mu_f = 1.6\Omega$ . For this set of parameters, we recover a similar scarring phenomenology as shown in the main text for the polarized state with  $\mu_0 = 1.68$ . However, we stress that the initial state considered here, i.e., the ground state of  $\hat{H}(\mu_i)$ , is now far from both the Néel and polarized states (the overlap with these states is on the order  $10^{-5}$ ). We emphasize that these values of  $\mu$  are not fine

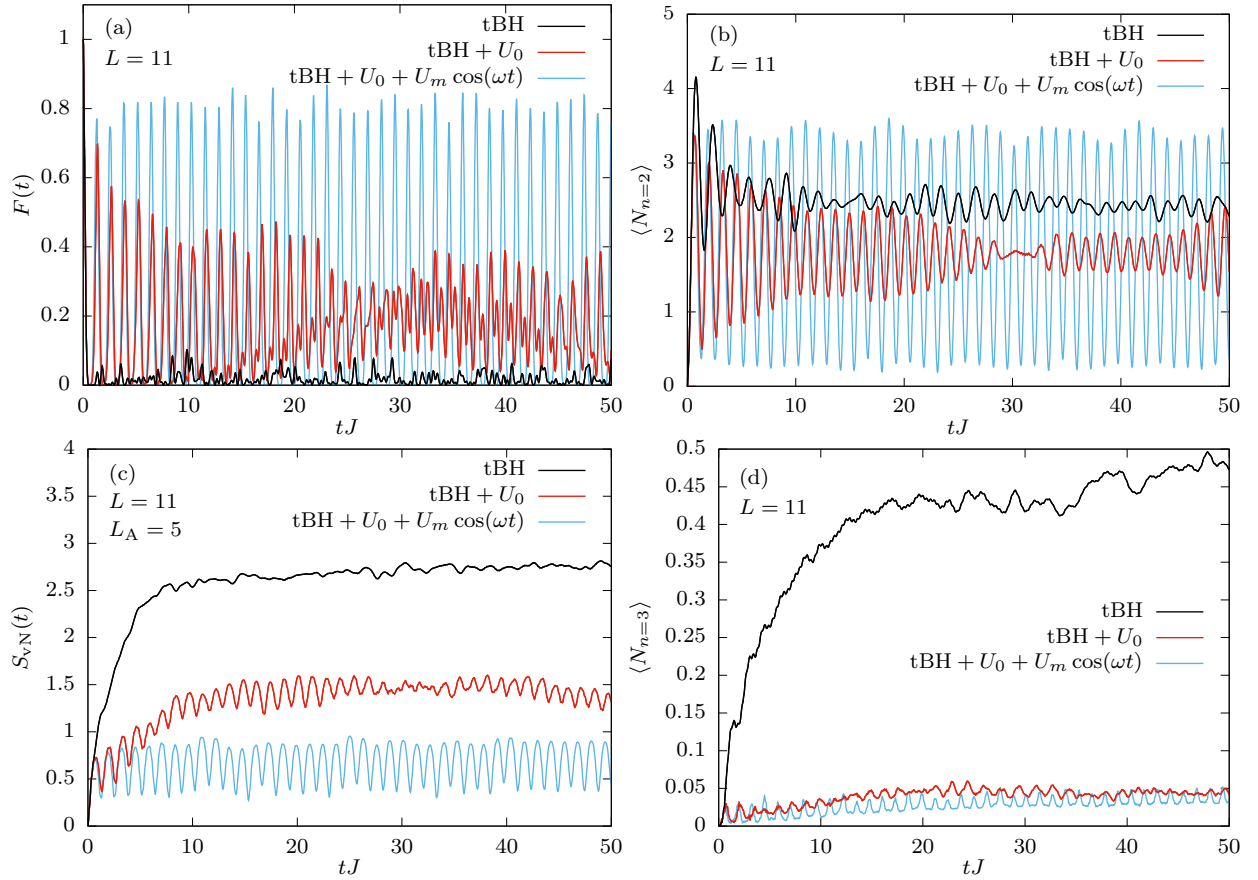


Figure S18. Comparison of dynamics in the tilted Bose-Hubbard model (black), with static detuning only (red), and with both static detuning and periodic driving (blue). System size  $L = 11$ , maximally 3 particles per site,  $J = 1$ ,  $\Delta = 16$ , driving parameters  $U_0 = -2.38$ ,  $U_m = 1.54$ ,  $\omega = 4.90$ . (a) Fidelity. (b) Expected total number of doublons  $N_{n=2}$ . (c) Entanglement entropy for subsystem size  $L_A = 5$ . (d) Expected total number of sites with three particles  $N_{n=3}$  (indicates the leakage from the PXP subspace).

1 tuned, and we find large regions of  $\mu_i$  and  $\mu_f$  leading to  
 2 scarring. 21

3 In Fig. S19 (a) we recover a dynamics close to what  
 4 could be observed for the polarized state with  $\mu = 1.68\Omega$ .  
 5 During the evolution, the state periodically transfers to  
 6 the polarized state and then returns to itself. The fre-  
 7 quency of revivals is approximately the same as that for  
 8 the polarized state evolved with the same static detuning  
 9  $\mu_f$ , but the revivals are more prominent. The overlap of  
 10 the  $\hat{H}(\mu_i)$  ground state with all the eigenstates of  $\hat{H}(\mu_f)$   
 11 is shown in Fig. S19(b). Comparing with the top states  
 12 having overlap with the polarized state at the same value  
 13  $\mu_f$  (red crosses) we see a similar pattern. More than that,  
 14 the same atypical eigenstates have a high overlap for both  
 15 states, but the phase is different in the two cases. This  
 16 is similar to what is observed with the Néel state and its  
 17 translated version for  $\mu_f=0$ . Both have the same over-  
 18 lap magnitude with each eigenstate, but the phases are  
 19 different. 31  
 32  
 33  
 34  
 35  
 36  
 37

## EFFECT OF DETUNING ON THE SPECTRAL STATISTICS OF THE PXP MODEL

In this section we show that the addition of finite detuning to the PXP model does not make this model integrable. We study the energy level spacings  $s_n = E_{n+1} - E_n$ , which we normalize to have  $\langle s_n \rangle = 1$ . For an integrable model,  $\{s_n\}$  should follow the Poisson distribution, while for a chaotic model we expect to see the Wigner-Dyson distribution. A convenient way to probe level statistics is by computing the so-called  $\langle r \rangle$  parameter [S19], defined as the average of level spacing ratios:

$$r_n = \frac{\min(s_n, s_{n-1})}{\max(s_n, s_{n-1})}. \quad (\text{S29})$$

For the Poisson statistics, we expect  $\langle r \rangle \approx 0.39$ , while  $\langle r \rangle \approx 0.53$  for Wigner-Dyson. In Fig. S20 we show that  $\langle r \rangle$  tends towards 0.53 as  $N$  increases, for all values of  $\mu$ . In general, as  $\mu$  becomes larger, the convergence is slower because the detuning approximately conserves the number of excitations. Beyond that, one can also notice two

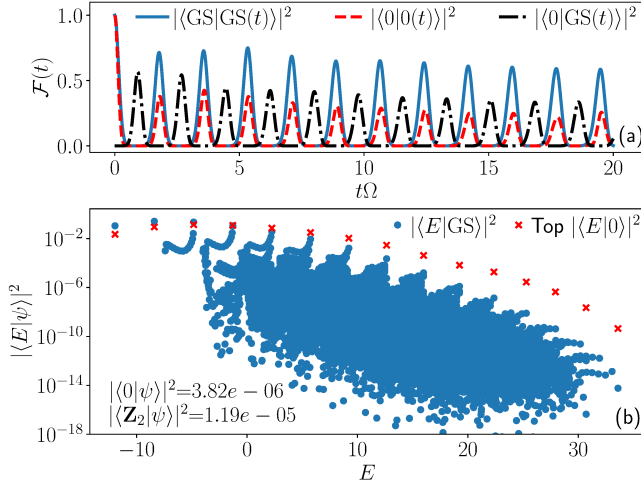


Figure S19. Emergence of many-body scarring by quenching the PXP model from  $\mu_i = -0.76\Omega$  to  $\mu_f = 1.6\Omega$  for  $N = 32$  spins in the  $k=0, p=1$  symmetry sector. The dynamics is very similar to that of the polarized state at the same  $\mu_f$ , with the overlap between the two suggesting that state transfer happens between them. The overlap between these two states and the eigenstates of  $\hat{H}(\mu_f)$  also shows similar tower structures.

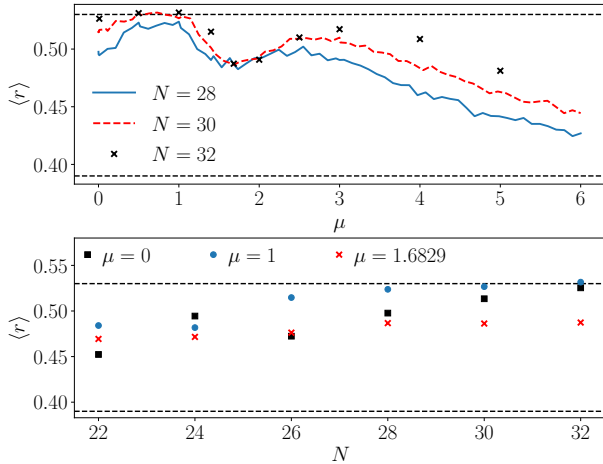


Figure S20.  $\langle r \rangle$  for the PXP model with various system sizes  $N$  and detuning  $\mu$ . For all values of  $\mu$  shown, the spectral statistics flows towards Wigner-Dyson value, as the  $\langle r \rangle$  parameter increases with system size. However the convergence is slower near  $\mu = 0$ ,  $\mu = 1.68$ , and in general as  $\mu$  becomes larger.

1 dips in  $\langle r \rangle$  at  $\mu = 0$  and  $\mu \approx 1.6$ , hinting that near these  
 2 values PXP is close to another integrable model. For  
 3 pure PXP this had been noted and previously investi-  
 4 gated with various other perturbations [S20].

5 The full distribution of the  $s_n$  is shown in Fig. S21 for  
 6  $\mu = 0, 1$ , and  $1.6829$  for  $N=32$  spins. In all cases, we  
 7 see that the distribution resembles Wigner-Dyson, even  
 8 though in the last case it is skewed towards zero.

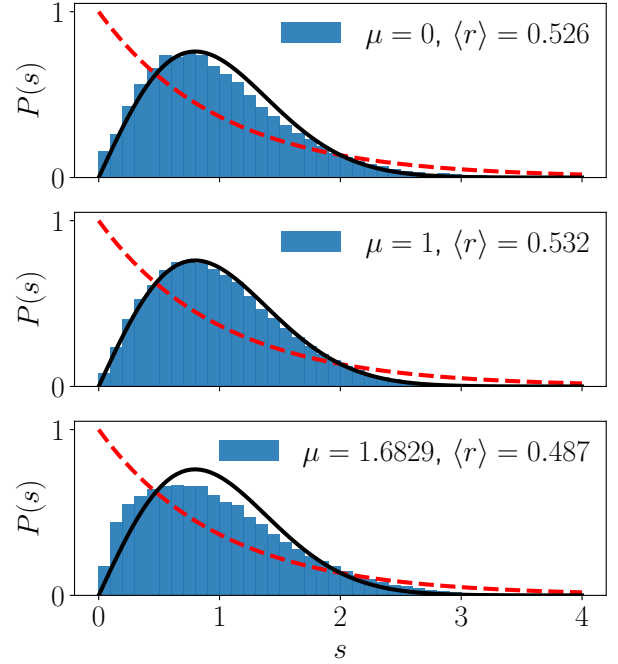


Figure S21. Distribution of the level spacings after spectrum unfolding for the PXP model with  $N=32$ . The solid black line corresponds to the Wigner-Dyson distribution and the dashed red line to Poisson. In all cases the distribution is close to Wigner-Dyson, even though for  $\mu = 1.6829$  it is skewed towards  $s = 0$ .

10 In conclusion, for any finite value of  $\mu$ , the PXP  
 11 model is non-integrable and its level statistics follow the  
 12 Wigner-Dyson distribution in a large enough system size.  
 13 Interestingly, the level statistics suggests a proximity to  
 14 an integrable model at the points where we find good re-  
 15 vivals due to scars: at  $\mu = 0$  for the Néel state and near  
 16  $\mu = 1.68$  for the polarized state. These results are in  
 17 accordance with the discrepancies observed between the  
 18 diagonal and canonical ensembles in Fig. S16.

## SYSTEM-SIZE SCALING OF THE REVIVAL FIDELITY

19 An important question concerns the stability of re-  
 20 vivals in the thermodynamic limit. In particular, due to  
 21 the cost of non-linear optimization, the driving param-  
 22 eters were obtained in relatively small systems, therefore  
 23 it needs to be checked whether the same parameters work  
 24 as well in large systems. For the calculations in this sec-  
 25 tion, we perform time evolution in large systems using the  
 26 TEBD algorithm implemented in TenPy package [S9], as  
 27 explained in Sec. .

28 Figs. S22 and S23 show the system size scaling of  
 29 the first three revival peaks for different initial states,  
 30 both with and without driving. The results were ob-  
 31 tained from numerical simulations of the tilted Bose-  
 32  
 33

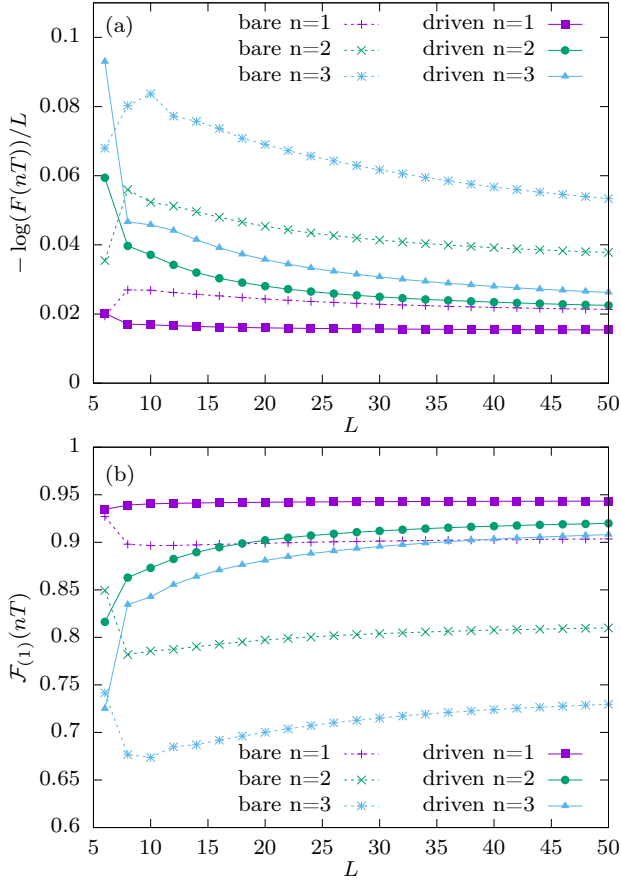


Figure S22. System size scaling of the first three revival peaks for the Néel state  $|\mathbb{Z}_2\rangle = |2020\dots 20\rangle$ . Driving parameters  $\omega = 3.85$ ,  $U_0 = 1.85$ ,  $U_m = 3.71$ . Dashed lines correspond to the bare case and the solid lines to the driven case. (a) Fidelity density. (b) Single-site fidelity.

1 Hubbard model, Eq. (S26), with open boundary conditions,  $\Delta/J = 16$ , and maximally 3 particles per site.  
 2 This particle number limit is a reasonable assumption since the periodically driven interaction strength  
 3  $U(t) = \Delta + U_0 + U_m \cos(\omega t)$  is large compared to the hopping amplitude  $J$ . In the case of global fidelity  $F(t)$ , we  
 4 plot the so-called fidelity density  $-\ln(F(nT))/L$ , where  
 5  $T$  is the revival period and  $n \in \{1, 2, 3\}$ . The single-site  
 6 fidelity  $\mathcal{F}_{(1)}(t)$  is a local quantity, so it does not need to  
 7 be rescaled by the system size  $L$ . We therefore simply  
 8 plot the peak heights  $\mathcal{F}_{(1)}(nT)$ .

12 For the Néel state  $2020\dots 20$ , the fidelity density is  
 13 expected to converge to a constant value in the limit of  
 14 large  $L$ . This is consistent with our results in Fig. S22(a),  
 15 where we plot the fidelity density after one, two and three  
 16 driving periods. The driving parameters are the same for  
 17 all system sizes,  $\omega = 3.85$ ,  $U_0 = 1.85$  and  $U_m = 3.71$ . Due  
 18 to the minus sign in the definition, lower fidelity density  
 19 corresponds to higher revival peaks and vice versa. As  
 20 can be observed in Fig. S22(a), periodic driving leads to  
 21 increased revivals over a broad range of system sizes and

22 there is no indication that this will change for  $L > 50$ .  
 23 The revivals are decaying with time, but the decay is  
 24 significantly slower when the driving is turned on. We  
 25 can thus conclude that periodic driving with these param-  
 26 eters both enhances and stabilises the revivals, even  
 27 in relatively large systems.

28 The scaling of the single-site fidelity can be observed  
 29 in Fig. S22(b). This experimentally measurable quantity  
 30 represents a tight upper bound for the global fidelity  
 31 when the system is initialized in a product state, see Sec-  
 32 tion . The results are similar to those for the global  
 33 fidelity. In all cases, the revival heights are rapidly con-  
 34 verging towards a constant value. Again, the revivals in  
 35 driven systems are significantly higher than those with-  
 36 out driving and the difference between them increases  
 37 with time.

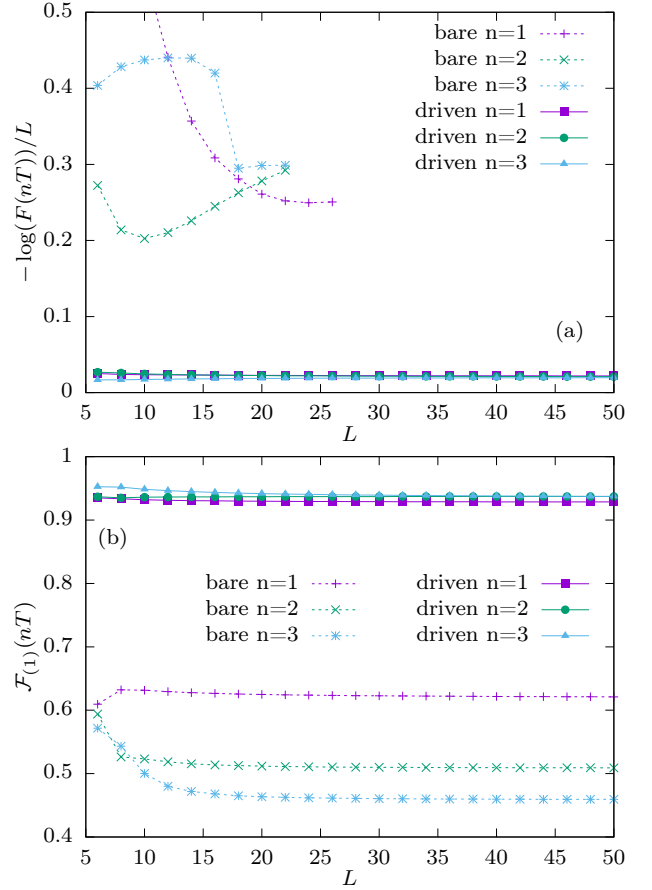


Figure S23. System size scaling of the first three revival peaks for the polarized state  $|111\dots 111\rangle$ . Driving parameters  $\omega = 4.90$ ,  $U_0 = -2.38$ ,  $U_m = 1.54$ . Dashed lines correspond to the bare case and the solid lines to the driven case. Data points are missing in cases where there are no local maxima. (a) Fidelity density. (b) Single-site fidelity.

The effects of periodic driving are even more striking  
 with the polarized state  $111\dots 111$  as the initial state,  
 as shown in Fig. S23. There are no notable revivals  
 in global fidelity when the driving is turned off. The

dashed lines in Fig. S23(a) correspond to irregular minor local maxima which are present in smaller systems. Even these local maxima disappear with increasing system size, which explains why some data points are missing. In contrast, driving with parameters  $\omega = 4.90$ ,  $U_0 = -2.38$  and  $U_m = 1.54$  produces very high revivals which do not decay, either with time or with system size. The single-site fidelity tells a similar story, see Fig. S23(b), however in this case there are revivals even in the absence of driving, consistent with dynamics of local observables in Fig. S12(b).

Finally, we note that the Néel and polarized states are the only two initial product states for which we were able to find optimal driving parameters that lead to robust revivals at late times. This is true both for the tilted Bose-Hubbard model, Eq. (S26) in the  $\Delta \approx U$  regime, and for the PXP model with a spatially uniform driving protocol. For other initial states, such as  $\mathbb{Z}_4$  state with an excitation on every fourth site or, equivalently, 20112011...2011 in the tilted Bose-Hubbard model, it is possible to stabilize a small number of revivals at short times. In contrast to the Néel and polarized states, these revivals are found to decay quickly with time as well as with system size.

---

\* yuanzs@ustc.edu.cn

† Z.Papic@leeds.ac.uk

‡ pan@ustc.edu.cn

[S1] I. Lesanovsky and H. Katsura, *Phys. Rev. A* **86**, 041601 (2012).

[S2] P. Fendley, K. Sengupta, and S. Sachdev, *Phys. Rev. B* **69**, 075106 (2004).

[S3] S. Sachdev, K. Sengupta, and S. M. Girvin, *Phys. Rev. B* **66**, 075128 (2002).

- [S4] K. Sengupta, “Phases and dynamics of ultracold bosons in a tilted optical lattice,” (2021), [arXiv:2109.02657](https://arxiv.org/abs/2109.02657) [[cond-mat.quant-gas](https://arxiv.org/abs/2109.02657)].
- [S5] C. J. Turner, A. A. Michailidis, D. A. Abanin, M. Serbyn, and Z. Papić, *Nature Physics* **14**, 745 (2018).
- [S6] C. J. Turner, A. A. Michailidis, D. A. Abanin, M. Serbyn, and Z. Papić, *Phys. Rev. B* **98**, 155134 (2018).
- [S7] S. Bravyi, D. P. DiVincenzo, and D. Loss, *Ann. Phys.* **326**, 2793 (2011).
- [S8] G. Vidal, *Phys. Rev. Lett.* **91**, 147902 (2003).
- [S9] J. Hauschild and F. Pollmann, *SciPost Phys. Lect. Notes*, **5** (2018), code available from <https://github.com/tenpy/tenpy>, [arXiv:1805.00055](https://arxiv.org/abs/1805.00055).
- [S10] J. C. Halimeh, R. Ott, I. P. McCulloch, B. Yang, and P. Hauke, *Phys. Rev. Research* **2**, 033361 (2020).
- [S11] F. M. Surace, P. P. Mazza, G. Giudici, A. Lerose, A. Gambassi, and M. Dalmonte, *Phys. Rev. X* **10**, 021041 (2020).
- [S12] D. Bluvstein, A. Omran, H. Levine, A. Keesling, G. Semeghini, S. Ebadi, T. T. Wang, A. A. Michailidis, N. Maskara, W. W. Ho, S. Choi, M. Serbyn, M. Greiner, V. Vuletić, and M. D. Lukin, *Science* **371**, 1355 (2021).
- [S13] N. Maskara, A. A. Michailidis, W. W. Ho, D. Bluvstein, S. Choi, M. D. Lukin, and M. Serbyn, *Phys. Rev. Lett.* **127**, 090602 (2021).
- [S14] H. Bernien, S. Schwartz, A. Keesling, H. Levine, A. Omran, H. Pichler, S. Choi, A. S. Zibrov, M. Endres, M. Greiner, V. Vuletić, and M. D. Lukin, *Nature* **551**, 579 (2017).
- [S15] B. Mukherjee, A. Sen, D. Sen, and K. Sengupta, *Phys. Rev. B* **102**, 075123 (2020).
- [S16] J. M. Deutsch, *Phys. Rev. A* **43**, 2046 (1991).
- [S17] M. Srednicki, *Phys. Rev. E* **50**, 888 (1994).
- [S18] Z. Yao, L. Pan, S. Liu, and H. Zhai, “Quantum many-body scars and quantum criticality,” (2021), [arXiv:2108.05113](https://arxiv.org/abs/2108.05113) [[cond-mat.quant-gas](https://arxiv.org/abs/2108.05113)].
- [S19] V. Oganesyan and D. A. Huse, *Phys. Rev. B* **75**, 155111 (2007).
- [S20] V. Khemani, C. R. Laumann, and A. Chandran, *Phys. Rev. B* **99**, 161101 (2019).

## Supplementary Files

This is a list of supplementary files associated with this preprint. Click to download.

- [SMQuantumManyBodyScar.pdf](#)